(12)

DNA-TR-81-170

RESULTS OF PLACES DATA ANALYSIS

C. W. Prettie
Berkeley Research Associates
125 University Ave., NE
P.O. Box 983
Berkeley, California 94710

1 September 1982

Technical Report

CONTRACT No. DNA 001-81-C-0130

APPROVED FOR PUBLIC RELEASE;
DISTRIBUTION UNLIMITED.

THIS WORK WAS SPONSORED BY THE DEFENSE NUCLEAR AGENCY
UNDER RDT&E RMSS CODE B322081466 I25AAXYX00006 H2590D.

Prepared for
Director
DEFENSE NUCLEAR AGENCY
Washington, DC 20305

Destroy this report when it is no longer needed. Do not return to sender.

PLEASE NOTIFY THE DEFENSE NUCLEAR AGENCY, ATTN: STTI, WASHINGTON, D.C. 20305, IF YOUR ADDRESS IS INCORRECT, IF YOU WISH TO BE DELETED FROM THE DISTRIBUTION LIST, OR IF THE ADDRESSEE IS NO LONGER EMPLOYED BY YOUR ORGANIZATION.

UNCLASSIFIED

SECURITY CLASSIFICATION OF THIS PAGE *(When Data Entered)*

REPORT DOCUMENTATION PAGE	READ INSTRUCTIONS BEFORE COMPLETING FORM
1. REPORT NUMBER: DNA-TR-81-170	2. GOVT ACCESSION NO.: AD-A130 933
3. RECIPIENT'S CATALOG NUMBER:	
4. TITLE *(and Subtitle)*: RESULTS OF PLACES DATA ANALYSIS	5. TYPE OF REPORT & PERIOD COVERED: Technical Report
	6. PERFORMING ORG. REPORT NUMBER: PD-BRA-82-278R
7. AUTHOR(s): C.W. Prettie	8. CONTRACT OR GRANT NUMBER(s): DNA 001-81-C-0130
9. PERFORMING ORGANIZATION NAME AND ADDRESS: Berkeley Research Associates, 125 University Avenue NE, P.O. Box 983, Berkeley, California 94710	10. PROGRAM ELEMENT, PROJECT, TASK AREA & WORK UNIT NUMBERS: Task I25AAXYX-00006
11. CONTROLLING OFFICE NAME AND ADDRESS: Director, Defense Nuclear Agency, Washington, DC 20305	12. REPORT DATE: 1 September 1982
	13. NUMBER OF PAGES: 86
14. MONITORING AGENCY NAME & ADDRESS*(if different from Controlling Office)*:	15. SECURITY CLASS *(of this report)*: UNCLASSIFIED
	15a. DECLASSIFICATION/DOWNGRADING SCHEDULE: N/A since UNCLASSIFIED

16. DISTRIBUTION STATEMENT *(of this Report)*

Approved for public release, distribution unlimited.

17. DISTRIBUTION STATEMENT *(of the abstract entered in Block 20, if different from Report)*

18. SUPPLEMENTARY NOTES

This work was sponsored by the Defense Nuclear Agency under RDT&E RMSS Code B322081466 I25AAXYX00006 H2590D.

19. KEY WORDS *(Continue on reverse side if necessary and identify by block number)*

PLACES
Propagation
Barium Cloud
Ionosphere
Striations
Phenomenology
Plasma Waves
Frequency Selective
Time Varying Impulse Response

20. ABSTRACT *(Continue on reverse side if necessary and identify by block number)*

The results of analyses performed to support PLACES data reduction and data interpretation are presented.

Beacon receiver measurements of the scattering of a 100 MHz pseudo-noise beacon signal BPSK modulated at a 10 MHz rate were made during an occultation by the structured IRIS ion cloud. The scattering produced features in the received St. George Island signal that are shown to be in good quantitative agreement with propagation effect predictions produced from an optically

DD FORM 1 JAN 73 1473 EDITION OF 1 NOV 65 IS OBSOLETE

UNCLASSIFIED

SECURITY CLASSIFICATION OF THIS PAGE *(When Data Entered)*

20. ABSTRACT (Continued)

derived model of the ion cloud extent. The features in the received data are also in qualitative agreement with the optical features in a coincident St. George Island photograph.

Neutral wind shear rate is determined in the optical analyses to be directed with a 351° azimuth with a 1.5 meter per second per kilometer of altitude magnitude.

Aircraft propagation measurements of the JAN ion cloud reveal a steady decay of the TEC until the cloud effects vanish at roughly 200 minutes after release. The following mechanism is proposed to explain late time barium cloud decay: Barium ions are removed from the ion cloud as current carriers and are replaced by molecular air ions which quickly recombine. The mechanism is found to be highly efficient.

The kHz frequency spurs in the NRL density probe data from JAN are briefly investigated. The spur frequency is found to have no clear-cut dependence on local density, is not confined to the ion cloud region, and at times two spurs are visible in the data.

PREFACE

The author would like to acknowledge the dedicated efforts of John R. Ferrante, who was responsible for the extensive and painstaking optical data reduction efforts that served as a backbone for Section 2, and the inspired efforts of S.Y. Frank Chu who was responsible for the numerical simulation work, including the free-space potential solver, reported in Section 3. The author would also like to thank Ed Szuszczewicz of NRL for extending the opportunity of processing his JAN data and C.S. Lin of NRL for his kind assistance in tape format decoding.

Throughout the effort the author has benefitted extensively from interactions and discussions with Dr. James M. Marshall, Wayne Solbrig, Jeff Lehman and Gary Elston of ESL; Dr. Lewis M. Linson of SAI; Dr. Victor Gonzalez, Dr. Dan McDaniel and Richard King of SRI International; Dr. Wally Boquist of TIC; Dr. Joseph Workman of BRA; Major Leon Wittwer of DNA; Dr. Ralph Kilb, Dr. William White and Dr. Robert Stagat of MRC and Dr. Morris Pongratz of LANL.

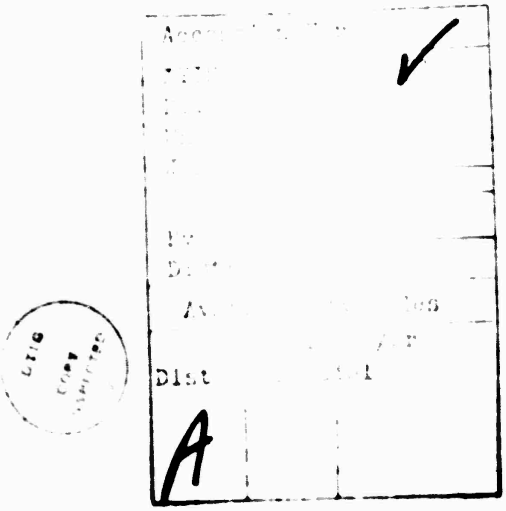

TABLE OF CONTENTS

LIST OF ILLUSTRATIONS

LIST OF ILLUSTRATIONS (Continued)

LIST OF ILLUSTRATIONS (Continued)

SECTION I

INTRODUCTION

The PLACES experiment was performed with two primary purposes. First, experimental verification of propagation relations which are used to specify the time-of-arrival spread and jitter effects expected on pseudo-noise PSK spread spectrum systems in HANE environments was desired. Second, measurements of the late time phenomenology were desired to address phenomenological issues of structured ion cloud evolution. BRA assisted ESL and other DNA community participants in the reduction and assessment of the PLACES data to address experimental goals. This report presents the results of the BRA effort.

The propagation relations for predicting pseudo-noise spread spectrum effects have a strong dependence upon the scattering geometry. In Section 2 a model for the IRIS cloud geometry during the first beacon occultation is developed. The beacon transmits a 10 MHz bandwidth 100 MHz pseudo-noise PSK signal to St. George Island and Cape San Blas receiving sites. The propagation effects observed in the St. George Island data are shown to verify the propagation predictions obtained from the model. As part of the geometric modelling, the occultation as viewed from St. George Island and a model for the neutral wind shear are also developed and presented in the section.

Section 3 focuses on explaining the decay of ion cloud TEC observed in the PLACES JAN aircraft data and in other barium release observations. A mechanism for this decay is presented. A numerical plasma cloud simulation which incorporates the important features of the mechanism has been performed and its results are also shown in this section.

An attempt was made to apply specialized software algorithms to the data from the NRL density probe flown through the JAN ion cloud (Szuszczewicz, 1981). The density probe data shows evidence of kHz plasma waves. While the specialized software did not perform as expected, important results relevant to any plasma wave explanations for these features were obtained and are briefly presented in Section 4.

The explanation of the experimental facets pertinent to the data interpretations is believed to be included in their discussion. For additional information about PLACES the reader is directed to Marshall, et al. (1981), McDaniel, compiler (1981) and the reports given in the Reference section.

SECTION 2

IRIS BEACON PROPAGATION MODELLING

The primary goal of the PLACES experiment is the verification of current propagation models for time-of-arrival spread and jitter effects. The ESL beacon launches performed during IRIS produced the first measurements of the time-of-arrival spread and jitter effects produced by striated barium clouds. The first payload launched achieved a very successful trajectory. Intense propagation effects were observed from both of the receiving sites at St. George Island and Cape San Blas. Propagation models for the effects observed at the St. George Island receiving site during the first beacon occultation are in good agreement with the observed geometry as discussed in this section.

Section 2.1 presents the modelling of the IRIS barium cloud geometry which was produced by integrating the optical data from many sites. This model is shown to be in good agreement with the FPS-85 radar data. Section 2.2 shows how the features observed in the received beacon signals agree with this cloud model. Predictive models are thus upheld. Section 2.3 shows how the propagation effects observed from St. George Island correspond to optical data from the same perspective. Section 2.4 presents the results of measurements of the neutral wind shear.

2-1 IRIS ION CLOUD GEOMETRY

During the design of the STRESS experiment, Dr. Gordon Best, then of AFCRL, expressed the thought that an excellent way to create a three dimensional barium cloud

model from optical data is to adopt a tomographic approach. Note that a tomographic approach requires data from multiple widely separated sites. In the instance when data is available from multiple sites the approach provides a good technique for producing a cloud model.

The IRIS ion cloud (8 December 1980) presented an opportunity to apply a rudimentary form of the tomographic technique. The optical data from six widely separated sites is available and has been used to describe the approximate position and extent of the ion cloud. A formal tomographic approach could be used to try to describe the structure of the interior of the cloud but the interior detail was felt not necessary for the propagation geometry model.

The display of three-dimensional models presents obvious practical problems. Since the scattering produced by the barium cloud is two-dimensional, one dimension, the field line direction, is superfluous and can be removed from the IRIS model to simplify model presentation. The formal manner to remove this dimension is to project the three-dimensional geometry onto a plane perpendicular to the field and to describe positions using two orthogonal distances from a given reference point. Another method is to project the geometry along geomagnetic field lines to a constant altitude and to describe positions using sub-latitude and sub-longitude coordinates. Because of the fortuitous geometry of the geomagnetic field in the Eglin AFB area the two techniques give close to identical results if the sub-latitude sub-longitude plot of the latter technique is made on a square grid. Distances on this grid represent roughly 100 kilometers per degree in the plane perpendicular to the field in both the N-S and E-W directions. Angles in the

plane perpendicular to the geomagnetic field are also kept true in this grid.

The optical data available at about 2345Z from six sites has been analyzed to find the azimuth and elevation of points near the extremity of the striated ion cloud. Table 2.1 details the sources and exact times of the data. These lines-of-sight have been projected onto a 155 kilometer altitude plane along geomagnetic field lines to produce the plot in Figure 2-1. Note that the choice of line-of-sight in the pictures is somewhat arbitrary since the cloud extremities are defined by field aligned streaks; however, any azimuth elevation pair from a field aligned streak projects into the same ray path in Figure 2-1.

The ray paths from the six sites define the cloud position and extent indicated in the figure. The cloud extent has been defined according to the C-6, Tyndall, and D-4 (Anclote) data which is believed to be the most reliable. The D-3 TV and St. George Island data is seen to be consistent with the resulting values. The aircraft data gives an inconsistent position for the south-eastern extremity of the cloud but the photograph from which the extremities were obtained is underexposed. The structure at the eastern extremity as determined from the C-6 data is very faint and this structure apparently did not register in the aircraft photograph.

The optical model of Figure 2-1 has been compared with RF data. The FPS-85 radar was run in an incoherent backscatter mode both to track the ion cloud and to diagnose its local density. Contours of the local density at 155 kilometers, as calculated by Dr. Victor Gonzales of SRII, are shown in Figure 2-2 plotted together with the optical

Table 2-1. Optical Data for IRIS Model

Site	Time	Source	Comment
C-6	2345:12	T.I.C. Photo	
Aircraft	2345:29	T.I.C. Photo	Underexposed
Tyndall	2344:53	T.I.C. Photo	
D-3A	2345:12	BRA Photo of SRII TV	
St. George Is.	2345:48	T.I.C. Photo	Figure 2-9
D-4	2345:28	LANL Image Intensified TV Photo	Northernmost extremity only, narrow field of view
D-4	2344:50	LANL Photo	Southernmost extremity only, underexposed

---

T.I.C. data from Dr. Wallace Boquist.

SRII TV data playback with assistance of Richard King and Dr. Dan McDaniel.

LANL data from Dr. Morris Pongrantz.

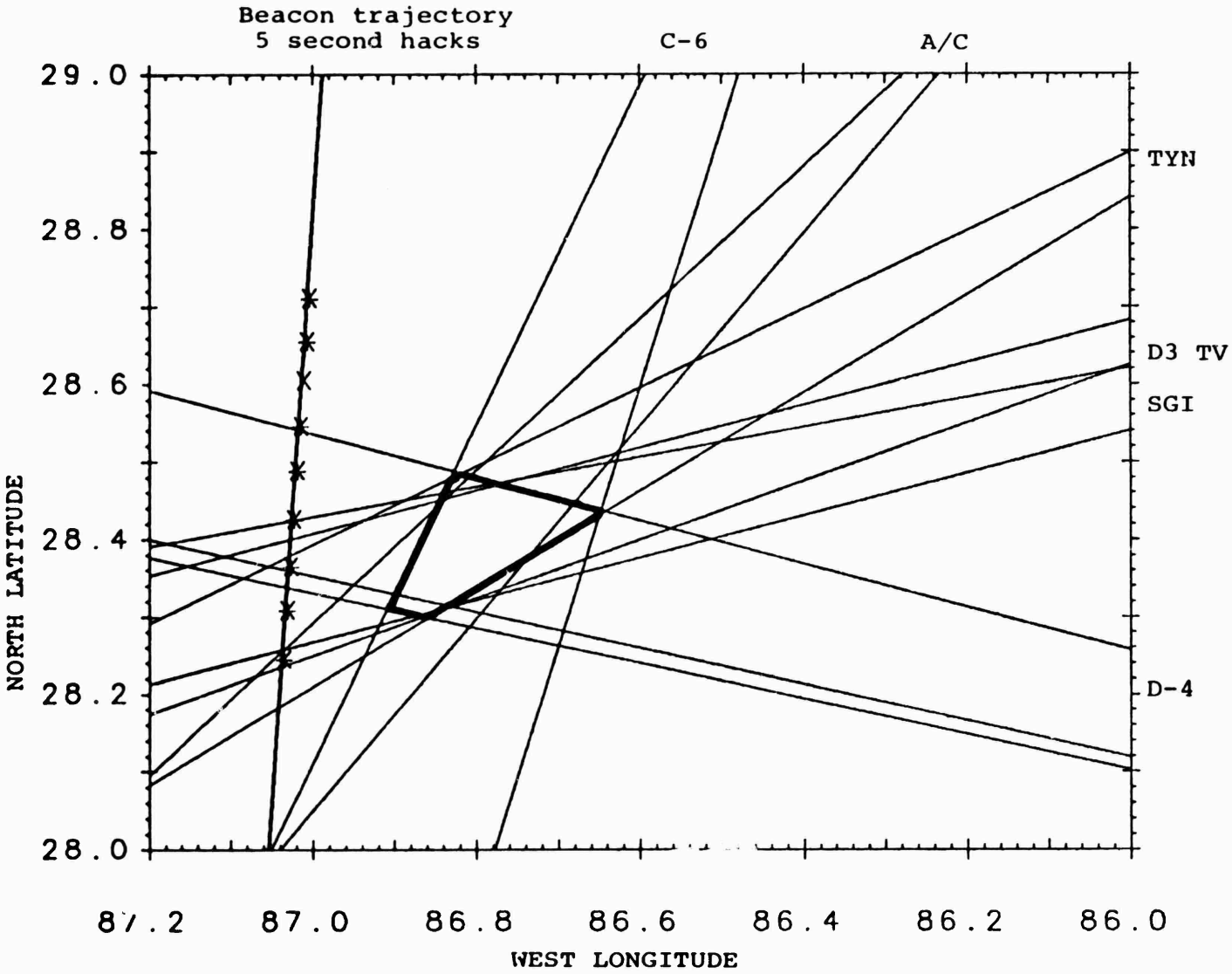

Figure 2-1. Optical model of IRIS position and extent referred to 155 km altitudes. The lines-of-sight to extremity of structure from numerous stations have been projected along field lines to 155 km altitude plane.

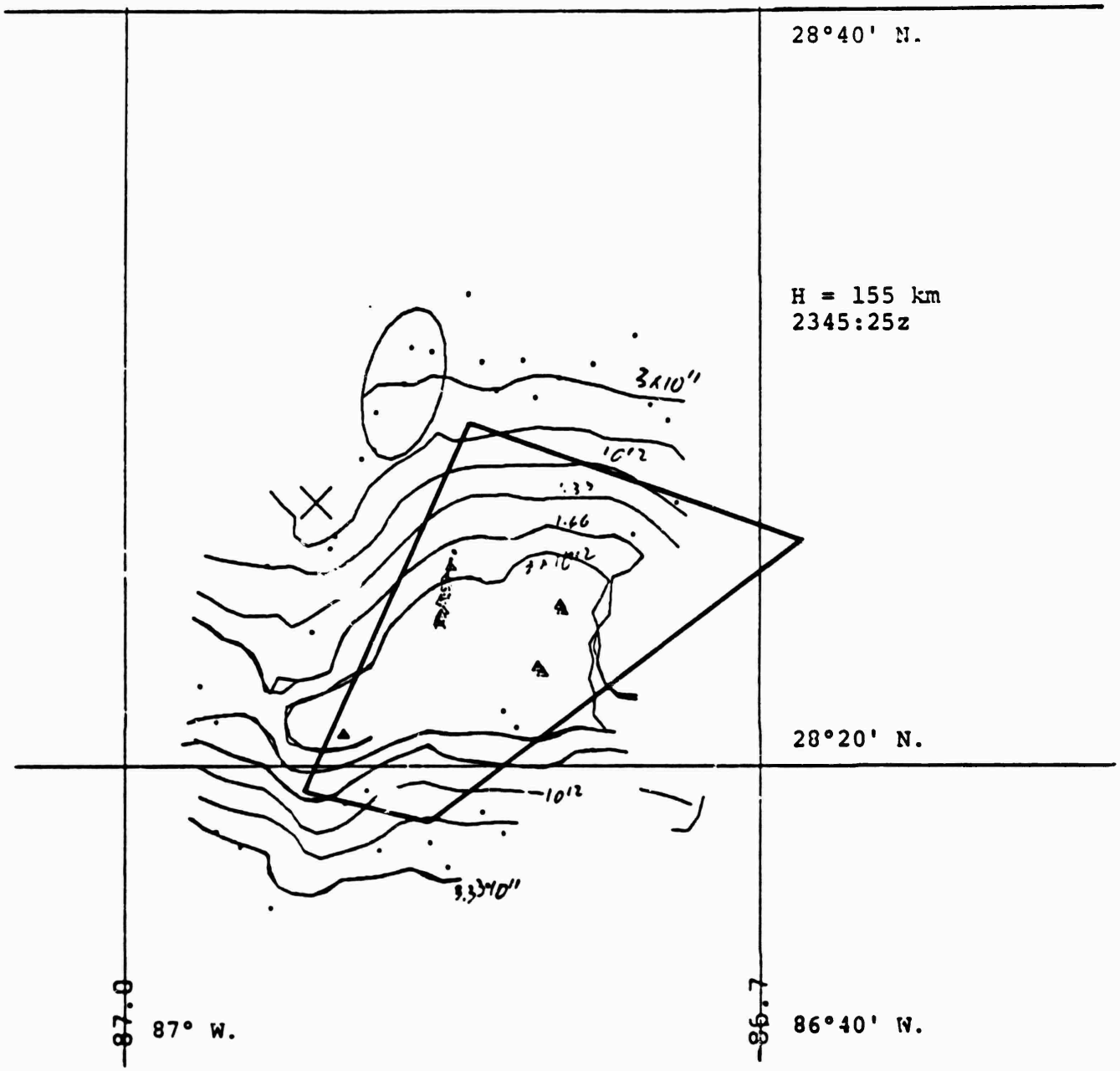

Figure 2-2. Overlay of IRIS optical model onto electron density contours determined by FPS-85 radar. Contour plot provided by Dr. Victor Gonzalez of SRI International.

results. The optically derived extent seems to be in good agreement with the 10^{12} electrons per meter cubed contour seen in the figure.

Figure 2-1 also illustrates the field line projected rocket trajectory. The markings on the trajectory represent 5 second intervals and the simple cross is a reference mark for the payload position at 2345:00. From the figure it is possible to infer a projected rocket speed of 1170 meters per second. The trajectory roughly makes a 75° angle with respect to the line-of-sight from St. George Island. The components of the velocity perpendicular to and parallel to the line-of-sight are thus 1130 meters per second and 300 meters per second respectively. Note that the 300 meter per second parallel component is in the direction of increasing range.

It is also possible to infer from the figure some of the distances relevant to the propagation effects. The projected distance from the payload to the ion structure is a maximum of 42 km and a minimum of roughly 10 km. The projected distance from the beacon to the rocket has been calculated to be roughly 192 km at the time of first occultation. Note that these distances are projected distances onto the plane perpendicular to the magnetic field. The distances in the three-dimensional geometry can be found by multiplying by the cosecant of the magnetic aspect angle, roughly 37° at the time of occultation.

The geomagnetic field lines used for the projection were determined from an IGRF field model (Trombka and Cain, 1974) provided by the Northwest branch of Physical Dynamics, Inc. Updated coefficients (Epoch 1980), as published in EOS, were provided by Dr. Lewis M. Linson of SAI and were

used in the model. The values for the field direction were cross-checked by comparing the computed geomagnetic zenith for JAN with that estimated visually from three A105 photographs provided by T.I.C. The JAN photographs were from a time when the JAN cloud ion structure was near the geomagnetic zenith. Agreement to within 1° was found. The IRIS dip and declination predicted by the model are 59.7° and 1.6° East, respectively.

2-2 IRIS PROPAGATION RESULTS

Propagation theory (Wittwer, 1979) indicates that time-of-arrival scattering effects are closely described by geometry considerations. When the spread and jitter effects become significant the theory predicts that time-of-arrival delay and carrier phase shifts are proportional to the dog-leg path increases in propagation distances. This strong geometric dependence is demonstrated not only in analytical propagation relations but also in the results of thin phase screen numerical propagation calculations.

The results of MRC pre-test numerical propagation calculations of the time varying impulse response expected from a smooth barium cloud dramatically demonstrates the geometric dependence of the impulse response effects (Figure 2-3). The wing features observed in the plot can be straightforwardly explained in terms of the dependence of the dog-leg path increase associated with angular scatter. Similar wing features are also visible in the ESL pre-test propagation calculations of a structured cloud seen in Figure 2-4. They are visible even though they are not as persistent as those in the smooth cloud.

Figure 2-5 illustrates the results of processing by ESL of the beacon data obtained from the St. George Island

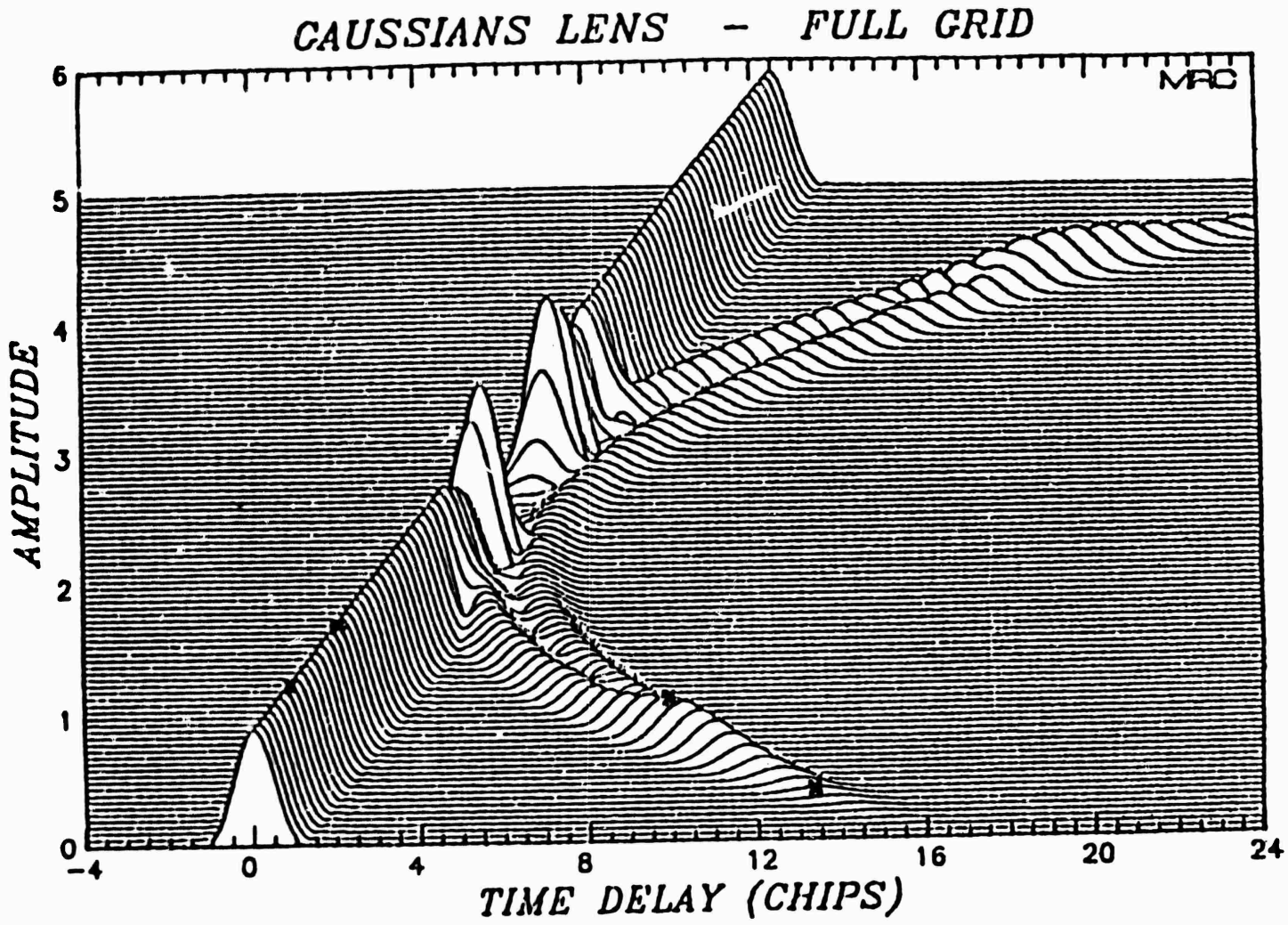

Figure 2-3. MRC pretest predictions. From letter to Capt. Wittwer titled: "Fifth Bimonthly Progress Report Contract DNA001-78-C-0364" 6 December 1979

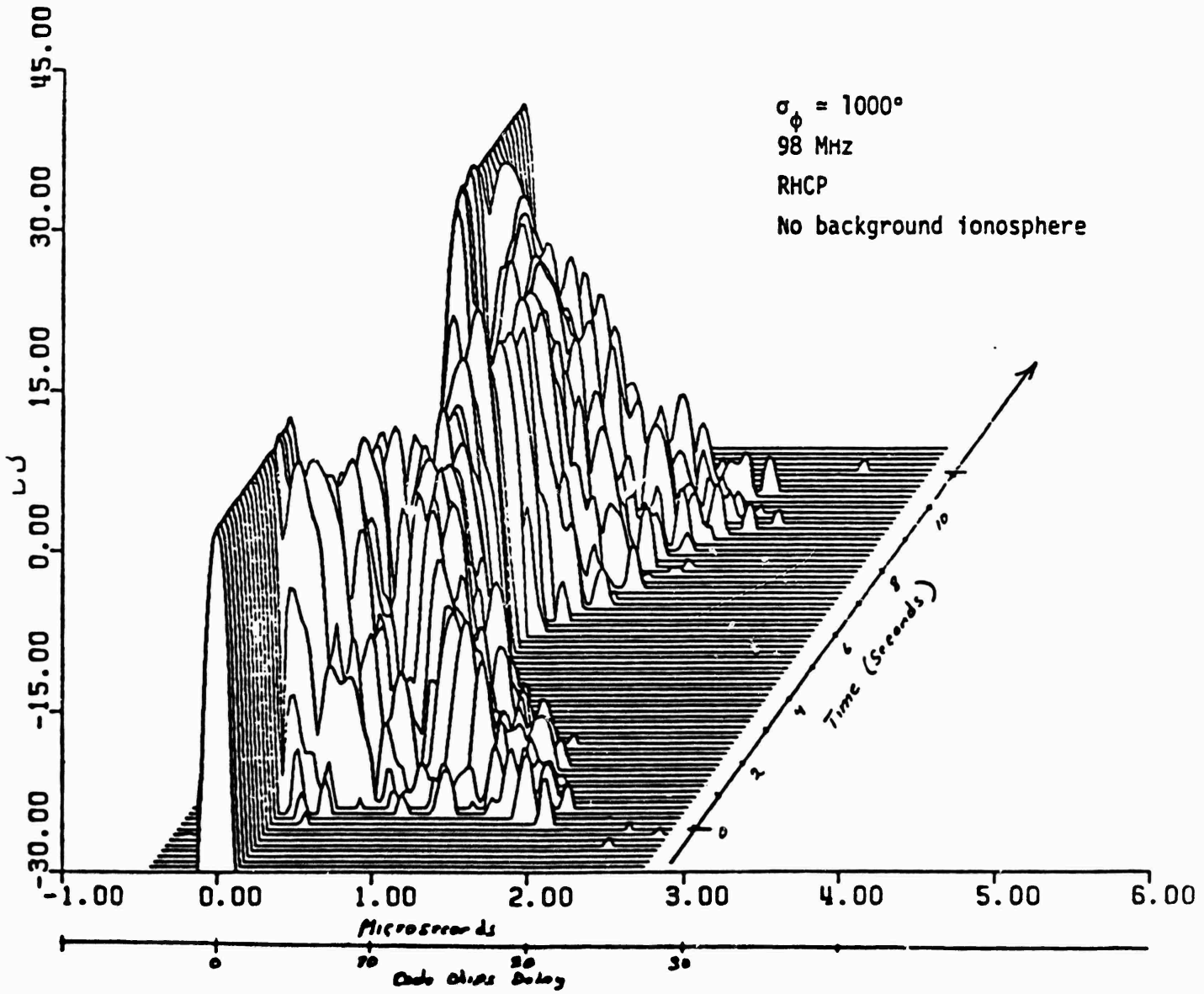

Figure 2-4 ESL pre-test predictions. From James M. Marshall, ESL, Preliminary Beacon Experiment Test Plan for PLACES 10 November 1980.

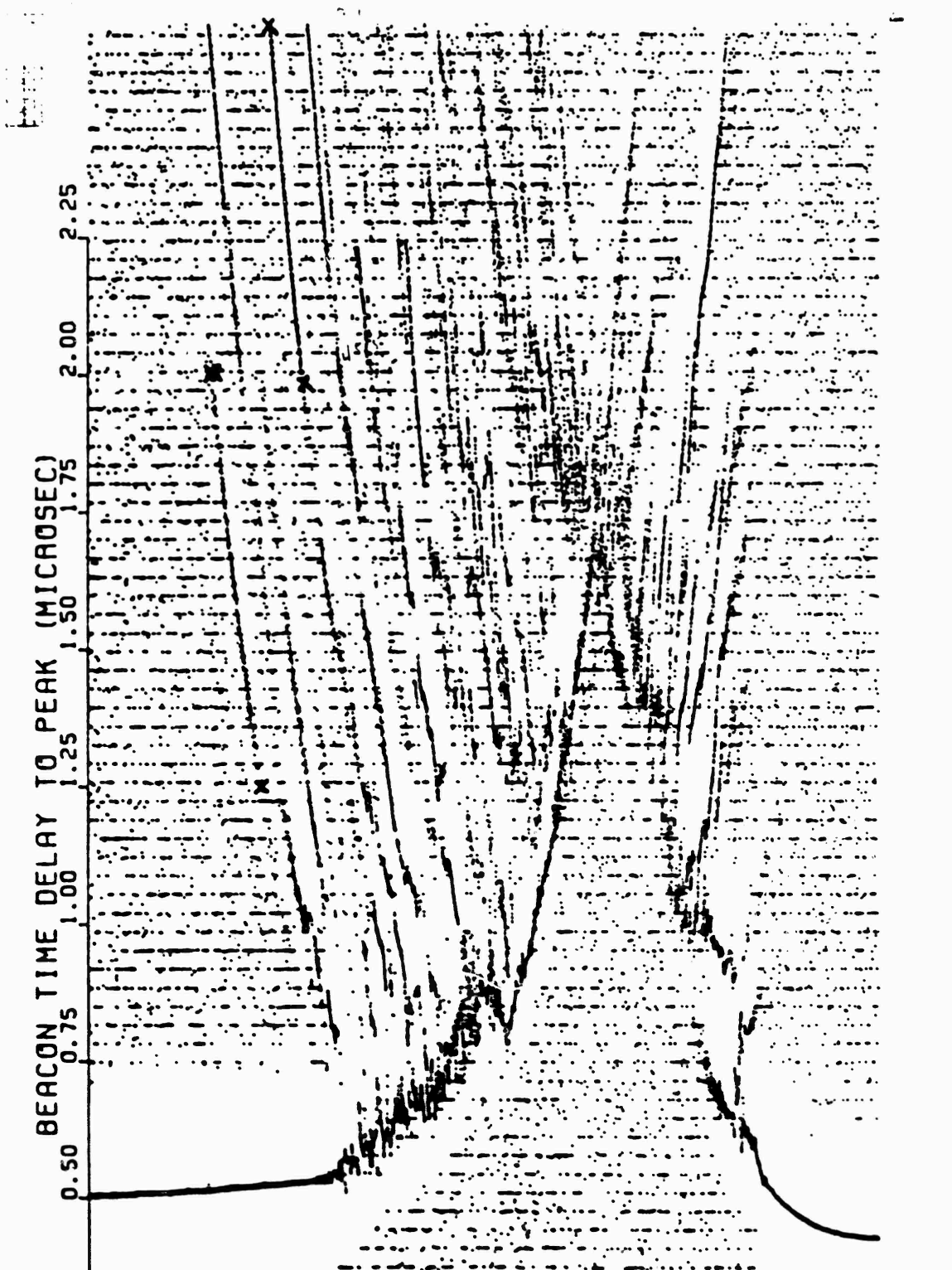

Figure 2-5. Time of arrival results for data from St. George Island first beacon measurement. Results provided by ESL.

receiver site during the first beacon occultation. The figure clearly demonstrates features which are qualitatively similar to the wing-like features seen in the pre-test predictions. Their quantitative agreement, which is demonstrated in this section, bears out the geometric nature of the effects.

The wing-like feature behavior can be predicted by considering the scattering geometry illustrated in Figure 2-6. The figure illustrates a beacon ray path which has been scattered off of a discrete object. At any instant in time the dog-leg increase in propagation distance d is

$$d = \sqrt{x^2 + z^2} - z$$

for x smaller than z, which is the case in small angle scatter,

$$d = \frac{1}{2}\frac{x^2}{z}$$

The rate change of dog-leg distance $\dot{d}$ in terms of both the x and z components of the beacon velocity is

$$\dot{d} = x\dot{x}/\sqrt{x^2 + z^2} + \dot{z}(z/\sqrt{x^2 + z^2} - 1)$$

Again considering small angle scatter with x smaller than z the expression becomes

$$\dot{d} = \dot{x}\frac{x}{z} - \frac{\dot{z}}{2}\left(\frac{x}{z}\right)^2$$

Since the $\dot{z}$ term is second order in x/z it can be neglected in many situations. The rate change of dog-leg delay is thus well approximated by

$$\dot{d} = \dot{x}(x/z)$$

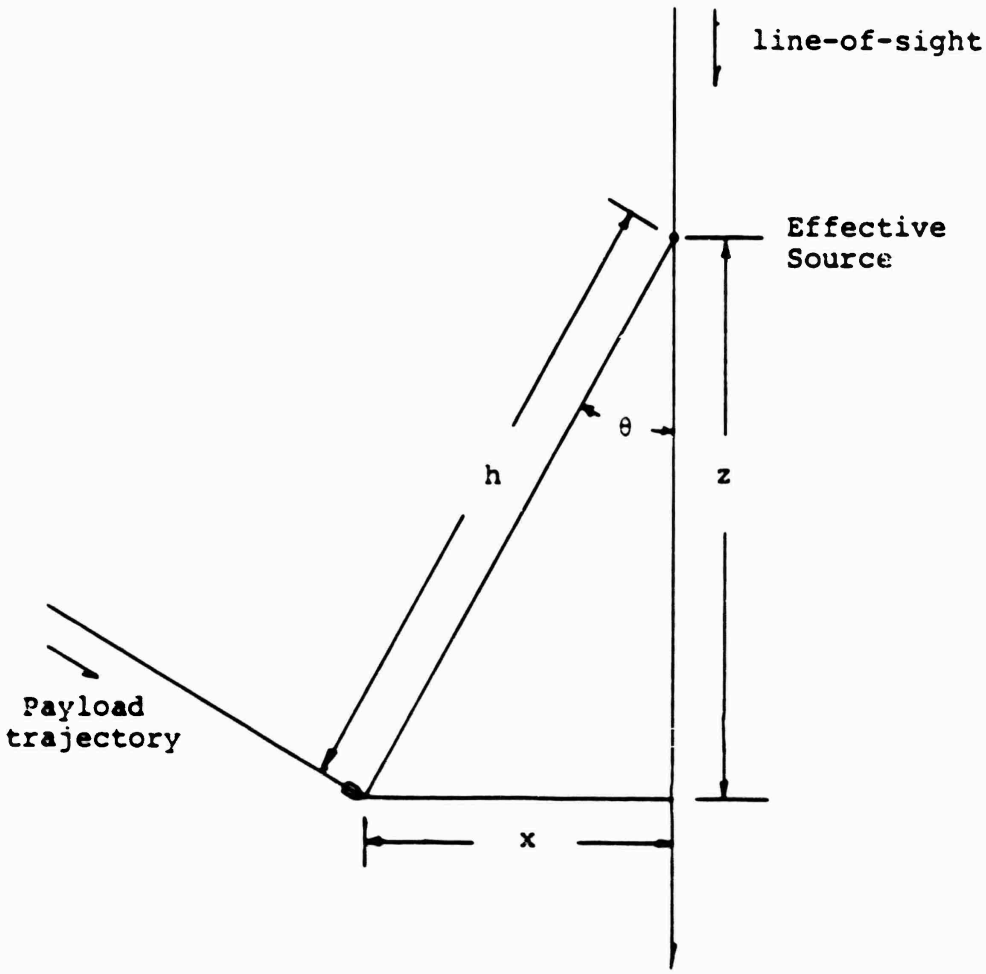

Figure 2-6. Idealized dog leg geometry between line-of-sight from St. George Island and beacon payload in plane perpendicular to field lines.

which for a constant x-component of velocity predicts a parabolic dependence for time delay τ in terms of time, t:

$$\tau = \frac{\dot{x}^2}{2\,cz}\,t^2$$

The qualitative nature of the wing features seen in Figures 2-3 thru 2-5 is thus explained.

It is possible to quantitatively check this relation by determining the value of z from the observed time dependence and comparing it with known or expected values. A good method for determining z is to fit the observed time delay versus time dependence with a parabola and to determine z from the coefficient giving the best fit. An alternative method is to estimate the coefficient of the parabolic dependence from the relation between the rate change of time delay and the time delay itself at a fixed point. The ratio of τ and $\dot{\tau}$ squared is found to be

$$\tau/\dot{\tau}^2 = cz/2\dot{x}^2$$

which can be used to find z and is useful in situations where the wing feature is of such brief duration that a parabolic fit would be difficult.

The latter method has been applied to the MRC propagation results shown in Figure 2-3 to evaluate z. A time delay change of .45 microseconds occurs over 1.8 kilometers between the points noted in the figure which have a mean delay of 1.0 microseconds. Assuming an arbitrary x-velocity component and a 3×10^8 m/s value for c gives a 107 kilometer value for z which is in good agreement with the known value of 100 kilometers. The wing features predicted by computational propagation simulations are thus in quantitative agreement with geometric arguments.

To apply the geometric relations to the PLACES data it is necessary to modify the dog-leg delay expression to accommodate the three dimensional nature of the problem. The direct and scattered ray path both extend a distance y out of the plane of Figure 2-6 where y is related to z through the magnetic aspect angle α:

$$y = z \operatorname{ctn} \alpha$$

The magnetic aspect angle is roughly 37° during the first beacon occultation viewed from St. George Island. (A magnetic aspect angle of 90° denotes broadside ray incidence.) The dog-leg delay becomes

$$d = \sqrt{x^2 + y^2 + z^2} - \sqrt{y^2 + z^2}$$

which reduces to

$$d = \frac{x^2}{2\sqrt{y^2 + z^2}} = \frac{x^2 \sin \alpha}{2z}$$

for small angle scatter. The delay rate is given by

$$\dot{d} = (x\dot{x} + y\dot{y} + z\dot{z})/\sqrt{x^2 + y^2 + z^2} - (y\dot{y} + z\dot{z})/\sqrt{y^2 + z^2}$$

For small angle scatter the $\dot{y}$ and $\dot{z}$ terms enter into the above expression in terms that are second order in x/z. Since they are both smaller than $\dot{x}$ they can be neglected giving for small angle scatter

$$\tau = \frac{\dot{x}^2 \sin \alpha}{2\, cz}\, t^2$$

$$\dot{\tau} = \frac{\dot{x}^2 \sin \alpha}{cz}\, t$$

and

$$\frac{\tau}{\dot{\tau}^2} = \frac{cz}{2\dot{x}^2 \sin \alpha}$$

To apply the geometric relations to the PLACES data it is also necessary to account for the fact that the distance from the beacon to the receiver sites is not infinite as assumed in the above analysis. Two modifications to the above relations are required. The more important for the results to be discussed is a moment arm correction to the x-component of the velocity. The effective velocity across the structure is given by the x-velocity corrected by the ratio of the distance between the receiver and the structure to the total distance between the receiver and the beacon payload. This ratio produces a roughly 10% decrease in the PLACES x-velocity which enters in the determination of z through a squared term.

The other modification that must be made is that the time-delay is now the result of a double dog-leg effect with the dog-leg terms between the scatterer and the beacon receiver now both contributing. By interpreting z obtained from the above expression as the distance resulting from a Lens law-like relation between distances to the scatterer the double dog-leg effect is accurately accounted for. This correction to z values partially offsets the moment arm correction to $\dot{x}$. Where the moment arm correction to the velocity produces correction terms involving the square of the moment arm ratio, including the double dog-leg effects reduces the composite correction factor to just the moment arm ratio. The final relations which allow the determination of z from the observed data are

$$\tau = \frac{z_t - z}{z_t} \quad \frac{\dot{x}^2 \sin \alpha}{2\, cz}$$

and

$$\frac{\tau}{\dot{\tau}^2} = \frac{z_t}{z_t - z} \quad \frac{cz}{2\dot{x}^2 \sin \alpha}$$

where z_t is the projected distance between the receiver and the beacon.

In the St. George Island data of Figure 2-5 the first two wing features show delay changes of .75 microseconds and .65 microseconds over intervals of 1.8 seconds and 1.3 seconds respectively. These features occur at mean delays of 1.13 microseconds and 1.84 microseconds respectively. The projected distance between the beacon and the receiver is approximately 192 kilometers, the value of $\dot{x}$ is 1130 meters per second, and the magnetic aspect angle is 37° from geometric considerations. The resulting values of z are 28.4 km and 31.5 km which are in very good agreement with the optically derived model discussed in Section 2.1. The wing features in the PLACES data are thus apparently in quantitative agreement with theory.

One other facet of the geometric interpretation of the data is the relationship between phase delay and time delay. If the cause of the time delay is primarily the increase in the geometric propagation distance then the phase shift associated with this effect should be proportional to it. Furthermore the doppler associated with any delay rate should be proportional to that rate. From the above relations between delay rate and delay the geometric approach predicts a parabolic dependence between the delay and the doppler measured at that delay:

$$f = \frac{\dot{d}}{\lambda} = \frac{\dot{x}}{\lambda}\left(\frac{z_t - z}{z_t z}\, 2\, c\tau \sin\alpha\right)^{1/2}$$

This dependence is observed in Figure 2-7 which shows further results from the ESL data processing. Figure 2-7 shows the doppler associated with a single wing feature plotted against the wing feature time delay. The fit parameter obtained by ESL to its dependence of $(37\ Hz)^2$ per microsecond of delay is in good agreement with the delay rate dependence observed above. It implies structure distances of 30.3 kilometers which is also in good agreement with the optical model.

Analytical expressions for the generalized power spectrum, $\Gamma(f,\tau)$, produce relations between doppler and delay similar to the above. The generalized power spectrum describes the power spectrum of the received signal at a fixed delay and is presented in Equation 46 of Wittwer (1979). The frequency of maximum intensity of the spectrum at a fixed delay is given by a relation which reduces to the above expression between f and τ. The spectrum is concentrated around this peak frequency which can thus be considered to be similar to a doppler effect. The generalized power spectrum has been calculated from the PLACES data. Figure 2-8 shows the peak of the generalized spectrum in frequency plotted versus delay as found from the generalized power spectrum of the St. George Island first beacon data. The result is very similar to the relation for the single wing feature shown in Figure 2-7. The agreement between this observed $\Gamma(f,\tau)$ dependence and the geometric knowns in the problem are also in good quantitative agreement.

2-3 BEACON OCCULTATION AS VIEWED FROM ST. GEORGE ISLAND

Figure 2-9 shows the IRIS ion cloud as viewed from St. George Island. The ion cloud image is from a transparency provided by Dr. Wally Boquist of T.I.C. For the purpose of presentation it was necessary to make a contact print of the

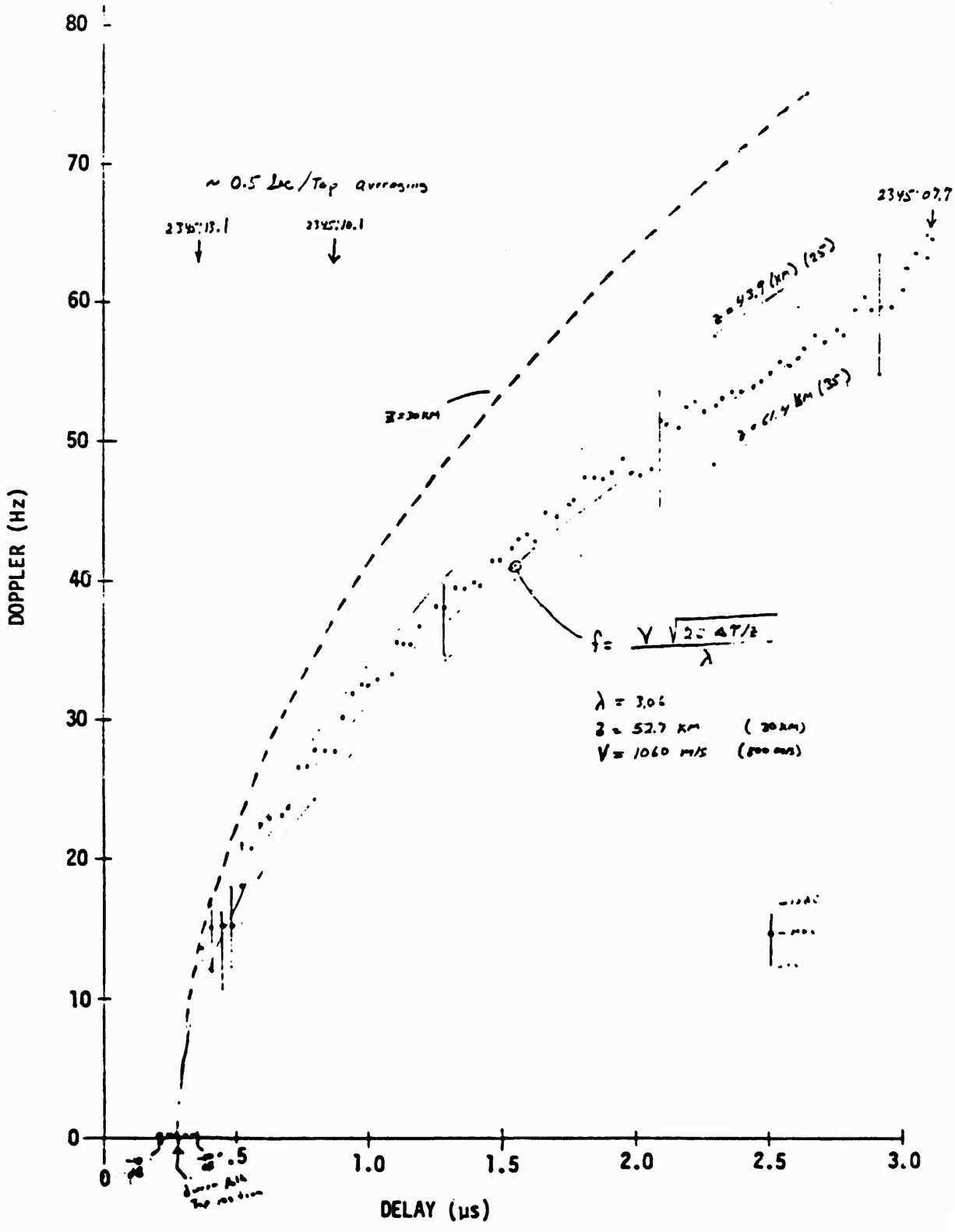

Differential Doppler Delay History of 1st Refracted Ray, St. George Island, Beacon 1

Figure 2-7. Single feature delay vs doppler. From ESL IR 190.

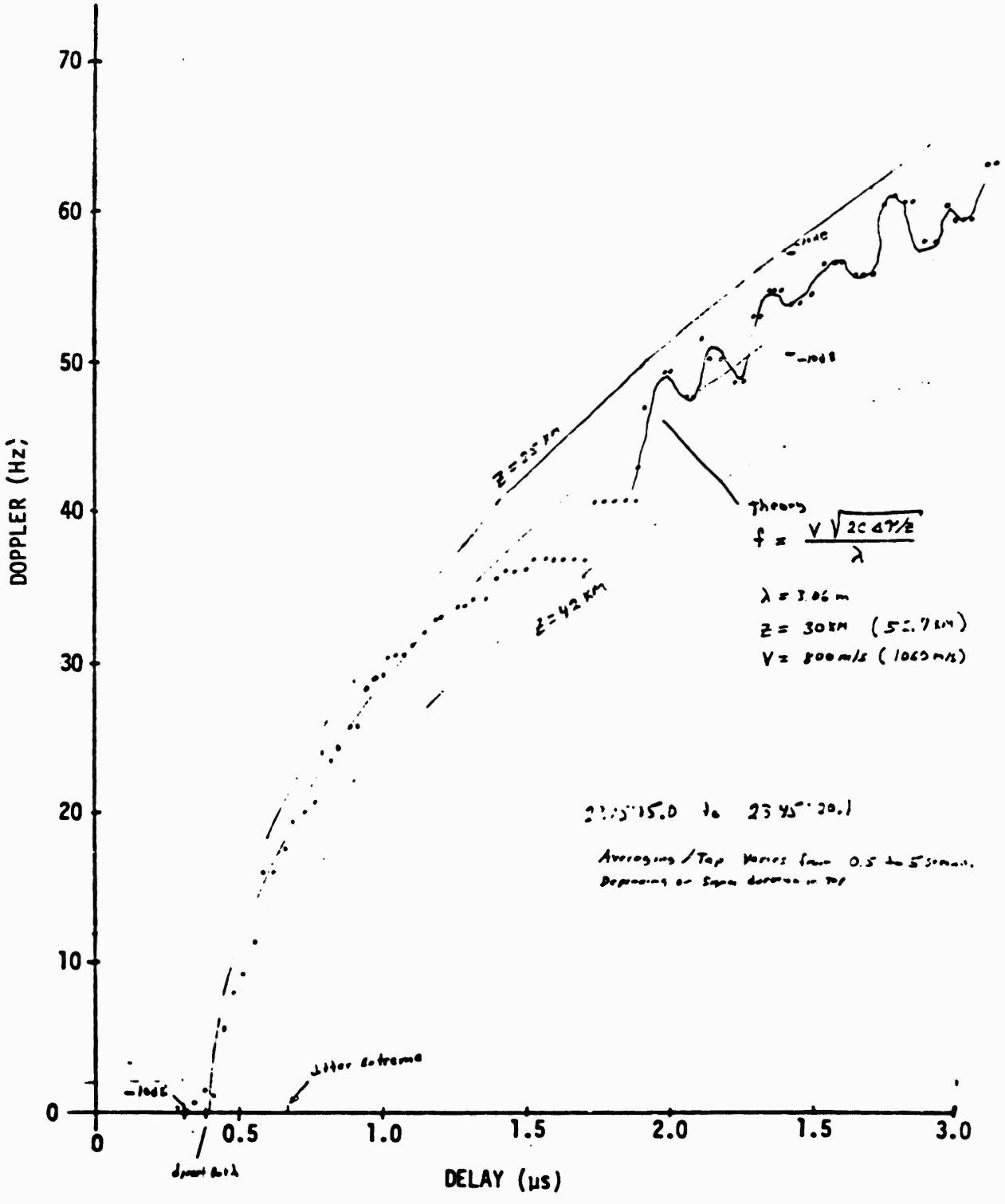

Differential Doppler Versus Delay, Many Refraction Rays, St. George Island, Beacon 1

Figure 2-8. Frequency of peak of generalized power spectrum at fixed value of delay versus delay. From ESL internal report IR 190 by J. Marshall, 1982.

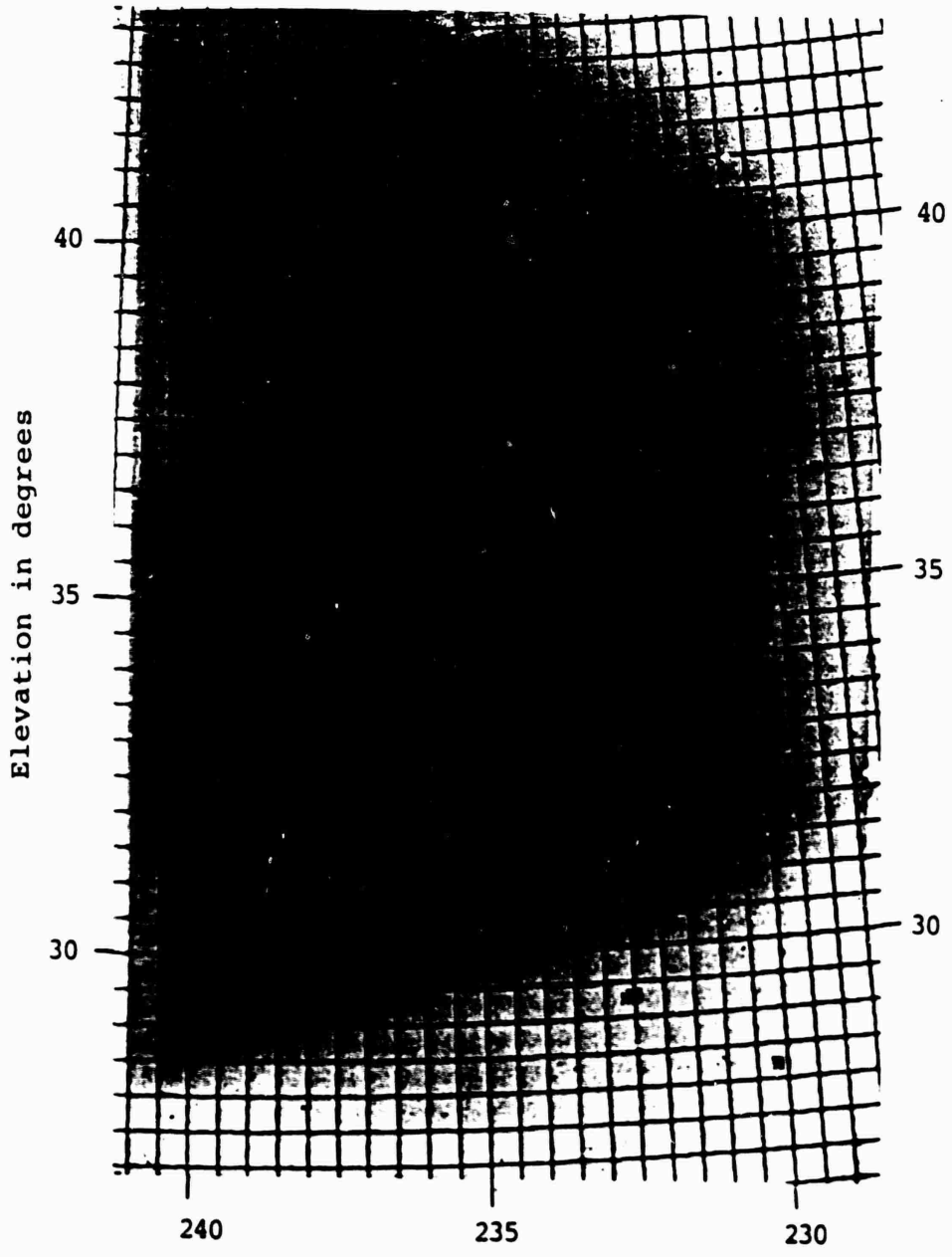

Figure 2-9. IRIS beacon occultation as viewed from St. George Island. The '×' is the beacon position at 2345:00. The'+' marks are 5 second hacks along the beacon trajectory. Asterisks '*' denote prominent star positions which were used to match the overlay with the photo.

transparency. As a result the figure shows a mirror image reversed and contrast reversed representation of the actual scene. Superimposed on the image is a plot of the azimuth and elevation contours and the beacon payload trajectory with five second hack marks.

Correlating features from the propagation results seen in Figure 2-5 with the optical features reveals qualitative agreement between the two. The first wing feature effect observed occurs when the beacon is outside the cloud. At roughly the same time that this feature intersects the direct path signal the beacon occultation begins optically. As the beacon moves further it passes through what appears optically to be strong structure, and strong scattering effects are correspondingly evident in the RF data. The point where the direct time delay is largest appears to be one of the brightest regions of the optical ion cloud. The beacon exits the cloud through what appears to be a fairly smooth region. The RF scattering effects are correspondingly decreased through this region. The RF exit time and the optical exit time appear to be in very good agreement. Thus many of the qualitative propagation features can be explained in terms of the optical data.

A brief description of the aximuth and elevation contour plotting technique, used not only in the plot of Figure 2-9 but also for analyzing all the other optical data, is appropriate. The azimuth and elevation contours are calculated by assuming that the film reproduces a flat plane projection of the sky. The relations for the x-y position of a point with specified azimuth and elevation, 'Az' and 'El' respectively, is:

$$x = A \sin(Az - Az_o) \cos El$$

$$y = A(\cos El_o \sin El - \cos(Az - Az_o) \cos El \sin El_o)$$

where 'El_o' and 'Az_o' are the respective boresight elevation and azimuth and where A is the scale factor between degrees and plot distance. The boresight azimuth and elevation are assumed to coincide with the center of the print. In the one case of the St. George Island photo this assumption is known to be wrong; however, the associated error in the resulting grid is small. The values of Az_o, El_o, and A are determined by adjusting the overlays to fit the known star positions. Typically three or four plot attempts were required to obtain a good fit. The American Ephemeris and Nautical Almanac, 1980 (1979), Webb's Atlas of the Stars (Webb, 1947) and the Yale Bright Star Catalog (Hoffleit, 1982) were used as sources for star positions. The latter is the most comprehensive, listing roughly 9,000 stars. The former lists roughly twelve hundred stars and is convenient in that precessional errors in position have been removed. Both the Yale Bright Star Catalog and the American Ephemeris and Nautical Almanac list star positions whereas Webb's Atlas gives star maps which were found generally useful. The contour calculation, rocket position calculation and star position calculation are all implemented in software. The overlay plots were found to be very useful for all of the optical data reduction.

2-4 IRIS WIND SHEAR

During all of the PLACES releases significant distortion of the neutral barium cloud occurred. Neutral cloud distortion also occured during the STRESS release DIANNE. Neutral cloud distortion is believe to be due to a linear altitude dependence

of the horizontal wind velocity which can be specified through a shear rate vector. This vector has significance to the barium cloud phenomenology and has been determined from the IRIS optical data.

Linson and Baxter (1978) attempted to determine the neutral wind shear rate for the STRESS release DIANNE with a multiple site algorithm. A similar technique is used herein to determine the shear rate for IRIS.

The IRIS neutral cloud distortion observed from all sites is roughly elliptical. The major axis of each ellipse points toward the accumulated wind shear. By measuring the angle that the major axis of each observed ellipse makes with the vertical direction two site solutions of the accumulated shear vector can be found for any pair of sites. If the data from more than two sites are available then multiple two site solutions can be compared to find the best fit. The shear rate is found by assuming that the accumulated shear vector is the result of a constant shear rate since the time of release.

Figures 2-10 thru 2-12 show the results of pairs of two site solutions obtained from three sites, namely D-4, the aircraft, and St. George Island at roughly 2341:00. The contours give error locus solutions. Each contour represents an additional 1° root sum of squares error in the angles read off the two photographs used for the solution. Note that a comparison of the results from all three pairs indicate that an azimuth of 351° and an elevation of 23° provides a good fit to the data with an r.s.s. error of roughly 2 1/2°. This accumulated shear distortion occurred over a 1600 second evolution time implying a shear rate of 1.5 m/s per kilometer of altitude at a 351° azimuth.

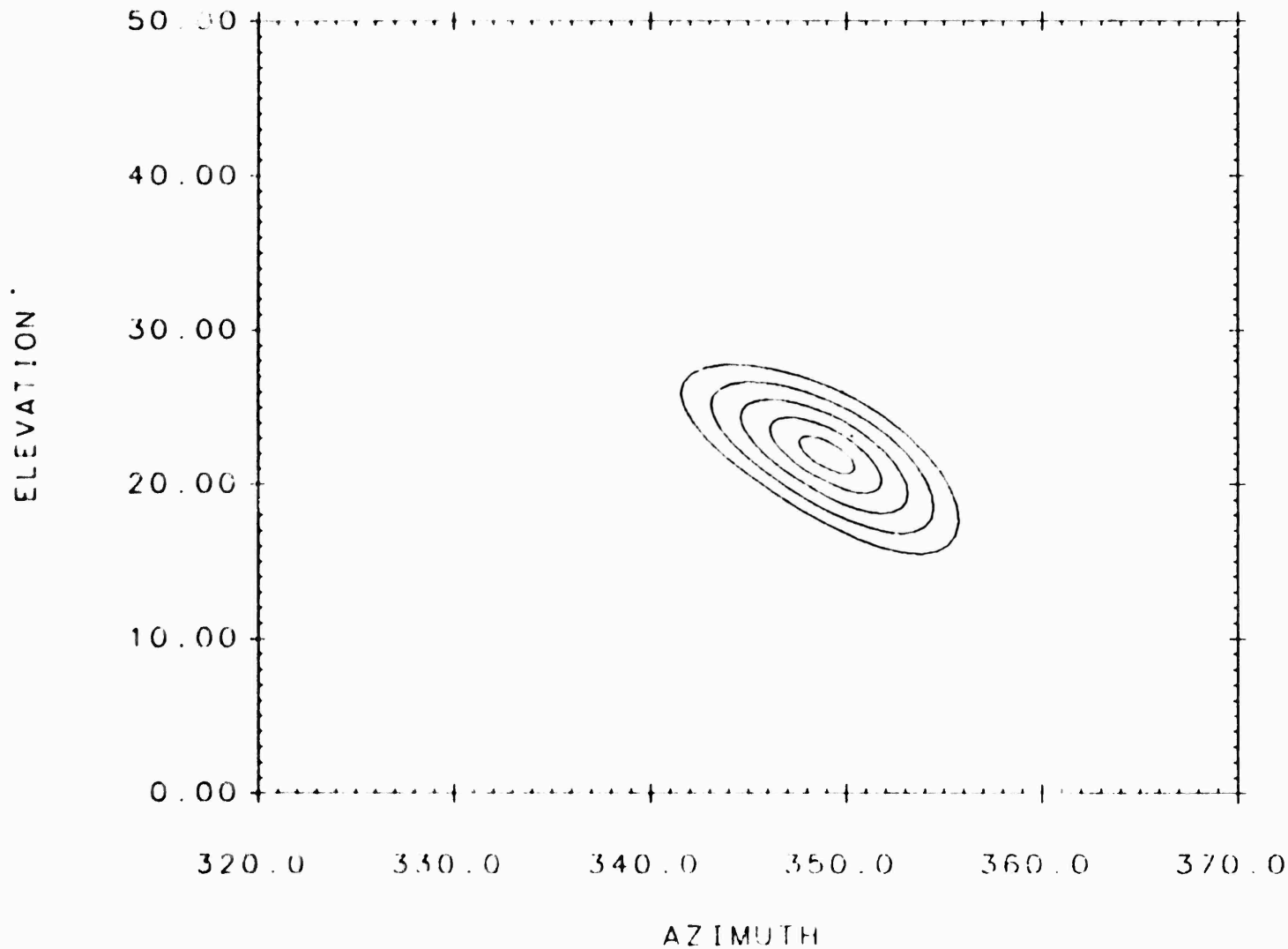

Figure 2-10. Orientation of major axis of neutral cloud elliptical distortion as inferred from data from D-4 2340:00 and the AFWAL aircraft 2341:03. The error locus are for 1° root sum of squares measurement error increments.

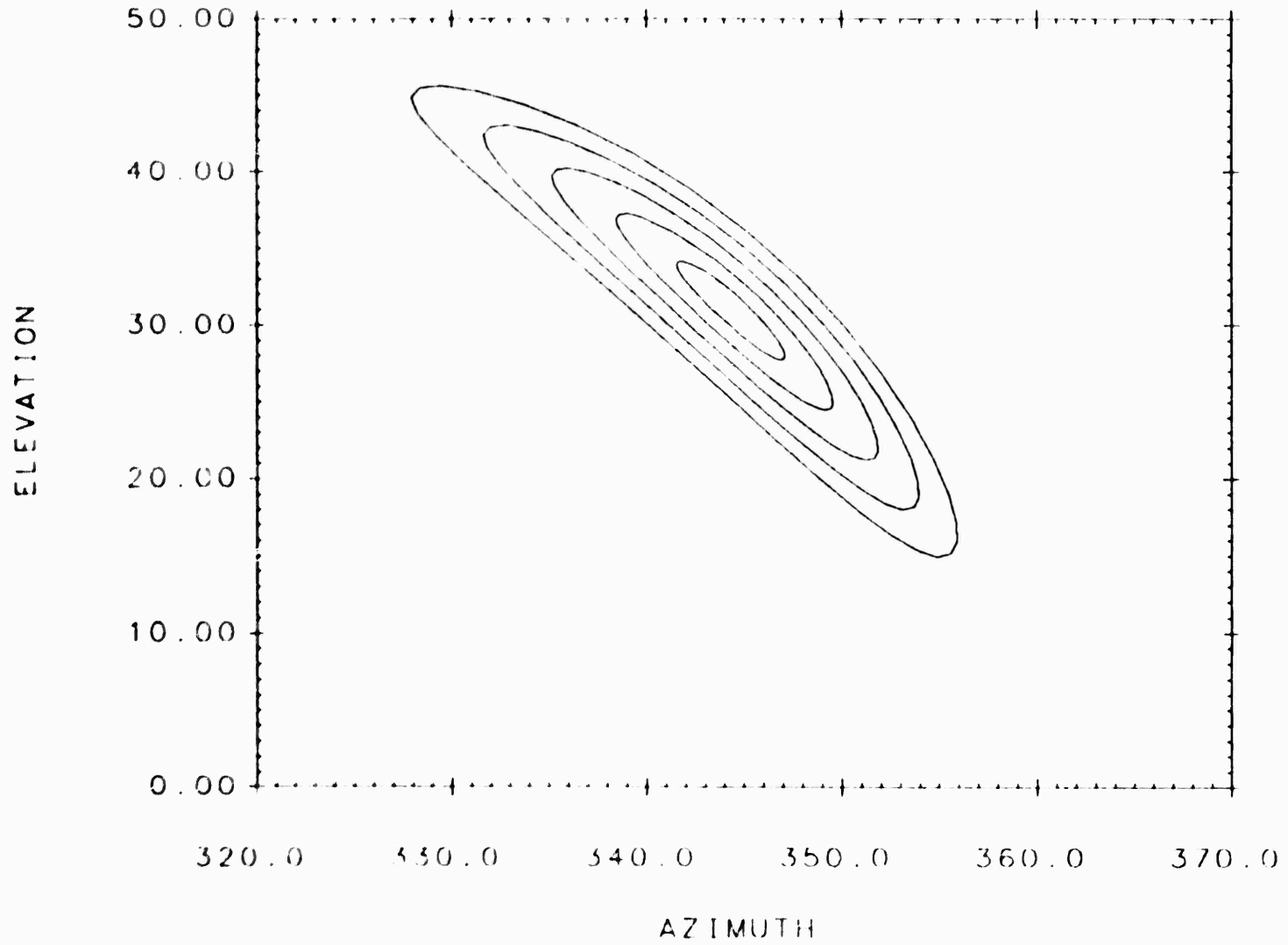

Figure 2-11. Orientation of major axis of neutral cloud from St. George Island photo at 2339:36 and the AFWAL aircraft photo.

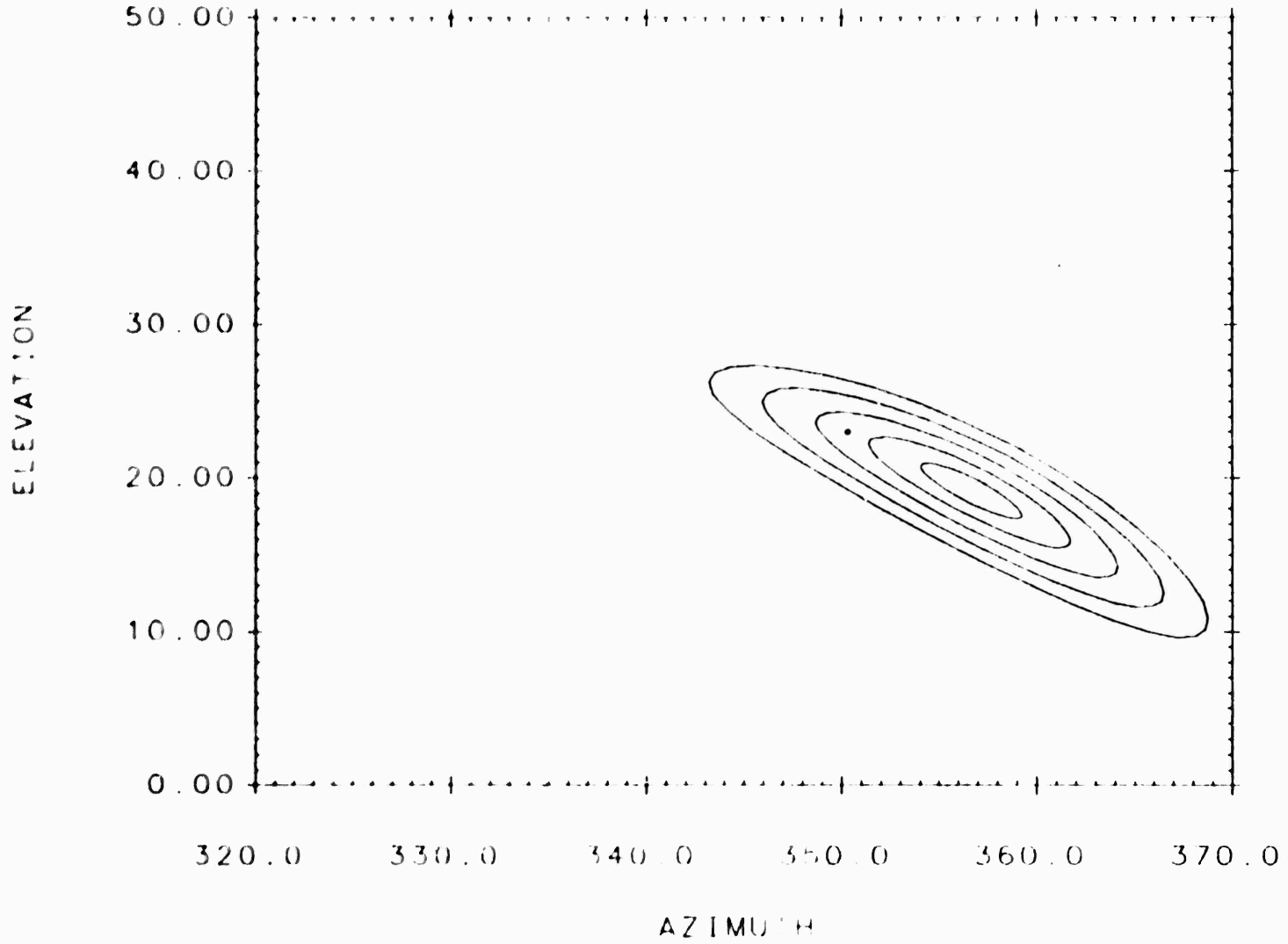

Figure 2-12. Orientation of major axis of neutral cloud from the St. George Island photo and the D-4 photo.

Neutral cloud distortion data is also available at 2345:00 from St. George Island, Tyndall and C-6. This data indicates a shear distortion vector with elevation of 21° and azimuth of 353°. The values imply a shear rate of 1.4 meter per second per kilometer at an azimuth of 353° which is good agreement with the 2341:00 data obtained from a different set of sites. The magnitude of the shear rate is also comparable to that found for DIANNE (Linson and Baxter, 1978) although the DIANNE shear rate vector was directed toward a 250° azimuth.

The magnitude and direction of the shear rate are of phenomenological interest. The magnitude of the shear rate indicates that the velocity differential over a 40 kilometer long striation would be roughly 60 m/s. This differential value is larger than the ion neutral slip. The direction of the shear rate is nearly perpendicular to the ion neutral slip and nearly parallel to the geomagnetic field. The former feature implies that different portions of the ion cloud could move in different directions according to which altitude had the highest Pedersen conductivity. The latter feature indicates that the components of the wind parallel to the field are trying to compress in altitude. Evidence of both ion cloud bending and compression in altitude is indicated in SRII data (McDaniel compiler, 1981) reproduced in Figures 2-13 and 2-14.

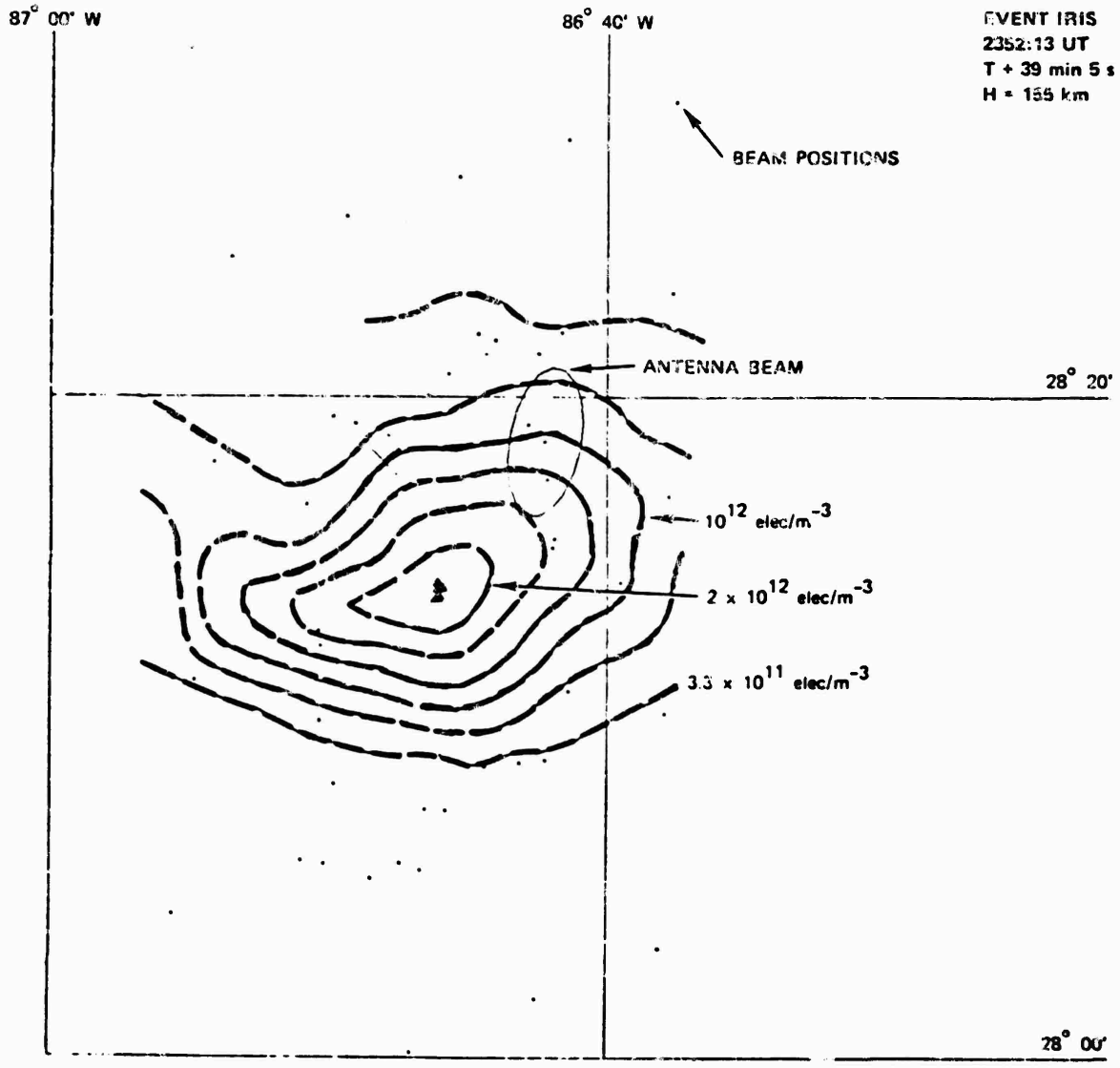

HORIZONTAL CONSTANT ELECTRON DENSITY CONTOURS OF EVENT IRIS AT T + 39 min

Figure 2-13. Density contours for IRIS suggesting bending of ion cloud. From Dr. Victor H. Gonzales "FPS-85 Radar Operations," p. 127 in McDaniel, compiler (1981).

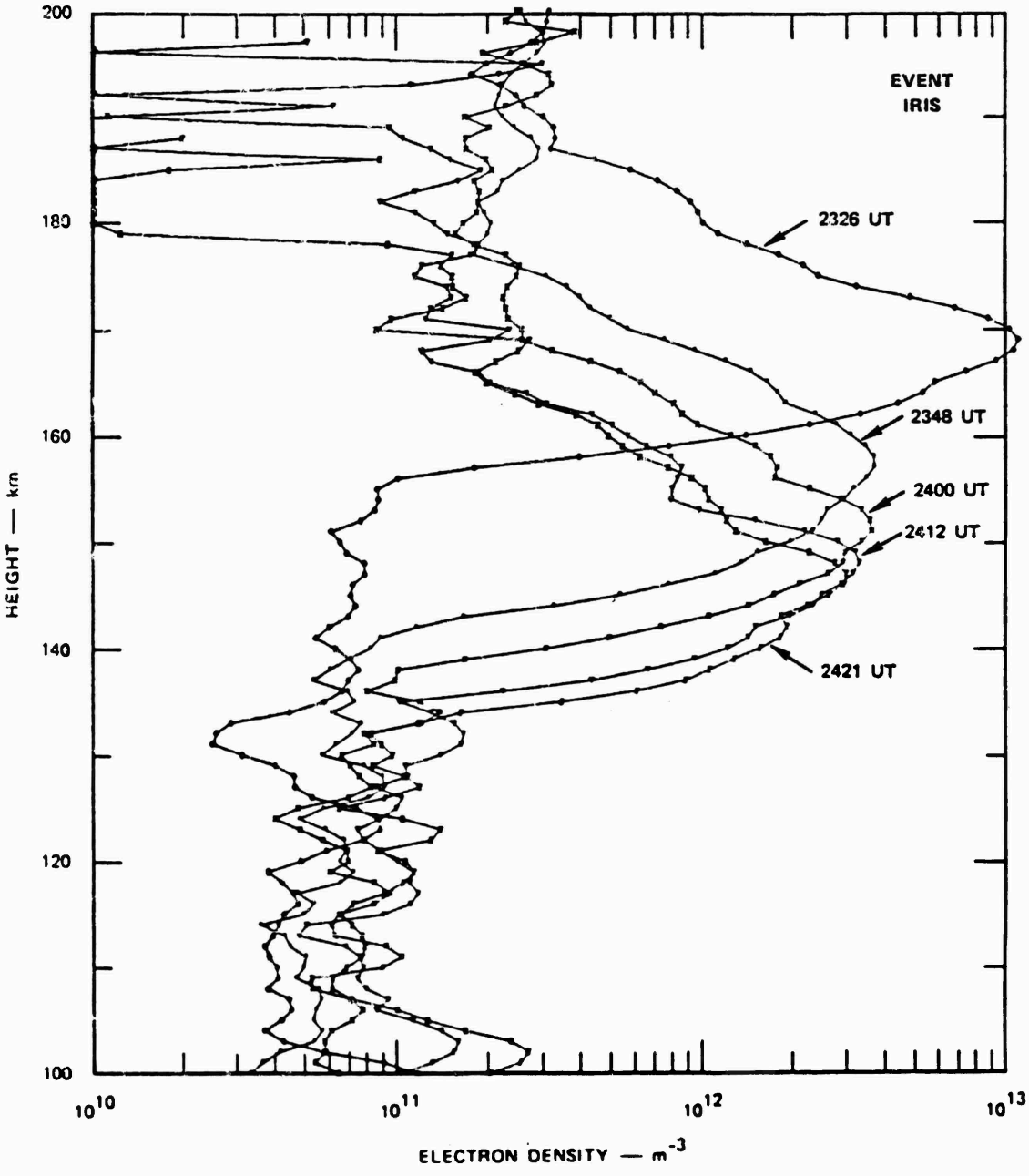

VERTICAL ELECTRON DENSITY PROFILES OF EVENT IRIS AT VARIOUS TIMES

Figure 2-14. IRIS density dependence with altitude. From Dr. Victor H. Gonzales "FPS-85 Radar Operations," p. 125 in McDaniel, compiler (1981).

SECTION 3

BARIUM CLOUD DISSIPATION MODELLING

The aircraft experiment performed during PLACES had the purpose of obtaining data on ion cloud phenomenology to late time. The ion cloud was tracked by radar until its presence could no longer be detected. The AFWAL aircraft was positioned by the radar so that RF signals from LES-8 would pass through the ion cloud. The data is then used as a diagnostic of ion cloud structure. Phenomenological issues such as the power spectrum of the measured ray path TEC fluctuations, its evolution with time, and the nature of barium cloud dissipation can then be addressed. A mechanism for barium cloud dissipation has been developed to interpret important features in these results as discussed in this section.

3-1 TEC DECAY OBSERVATIONS

The aircraft trajectories were flown during PLACES such that numerous passes were made through the LES-8 ion cloud shadow in a direction primarily perpendicular to the projected field lines (see Marshall, et al., 1981, for detailed plots). The peak phase shift measured on each pass is roughly proportional to the total electron content of the plasma cloud along the line-of-sight. While, in general, the aircraft passes will not cross the cloud at the point of maximum TEC on any one pass, a sufficient number of passes are performed so that the maximum TEC dependence with time is roughly approximated. Figure 3-1 shows the dependence derived by ESL from the JAN data (Marshall, et al., 1981).

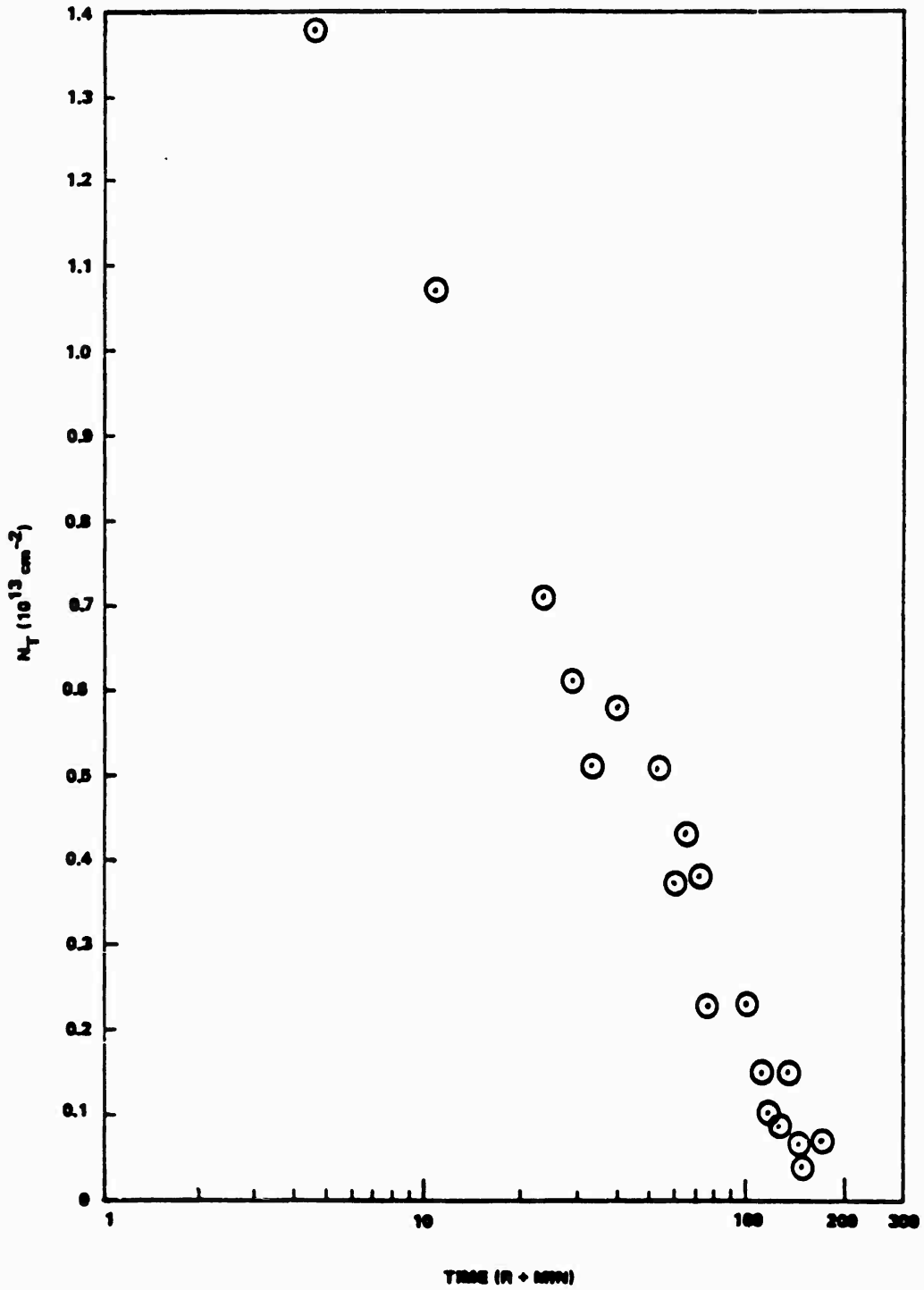

Figure 3-1. The decay of peak integrated electron content versus time after release observed in JAN. Reproduction of Figure 3-60 of Marshall, et al., (1981).

The JAN dependence indicates that the peak TEC of the barium cloud is decaying exponentially with time. The decay is seemingly smooth over an order of magnitude in time. This exponential decay is also observed in the STRESS data from DIANNE, ESTHER and FERN seen in Figures 3-2, 3-3, and 3-4. These plots suggest that the disappearance of barium cloud effects is due to a systematic logarithmic decay in the TEC. While it has been argued that this decay might be due to a systematic error in the radar positioning, the reproduction of this similar dependence in four releases argues that the decay is a bonafide phenomenon.

3-2 ION CLOUD DECAY

Ionospheric currents transverse to the geomagnetic field are carried by ions. It is very difficult to move electrons across field lines. The fact that currents are carried by ions leads to the mechanism of ion cloud decay believed to be operative in the STRESS and PLACES barium releases.

The relative motion of barium ion and neutral clouds and the associated distortion and structuring of the ion clouds is produced by a non-zero wind velocity in the frame of the ambient plasma. The neutral wind produces currents in the background ionosphere as well as intensified currents in the barium ion cloud. The barium ion cloud currents produce electric fields which cause the ion cloud motion through the ambient ionosphere toward the neutral cloud and subsequent ion cloud distortion. The magnitude of the current in the ion cloud can be determined from the relation

$$J = \frac{N}{\mu B} V_{slip}$$

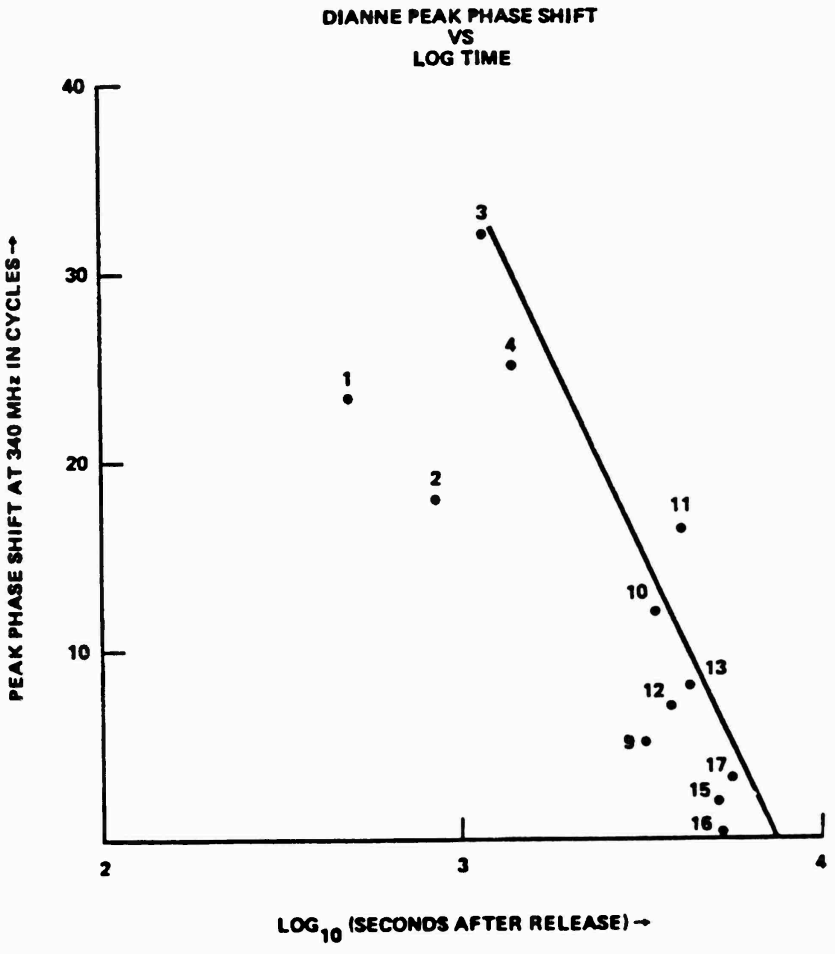

Figure 3-2. The decay of peak integrated electron content versus time after release observed in the DIANNE release of STRESS.

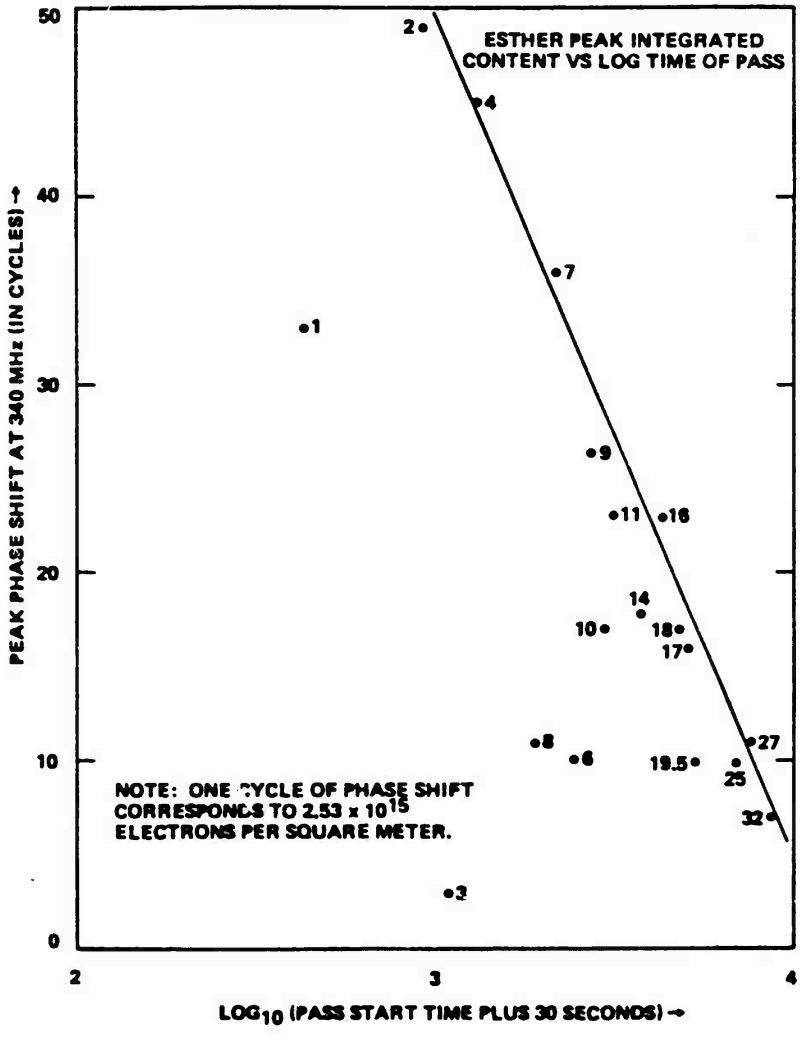

Figure 3-3. The decay of peak integrated electron content versus time after release observed in the ESTHER release of STRESS.

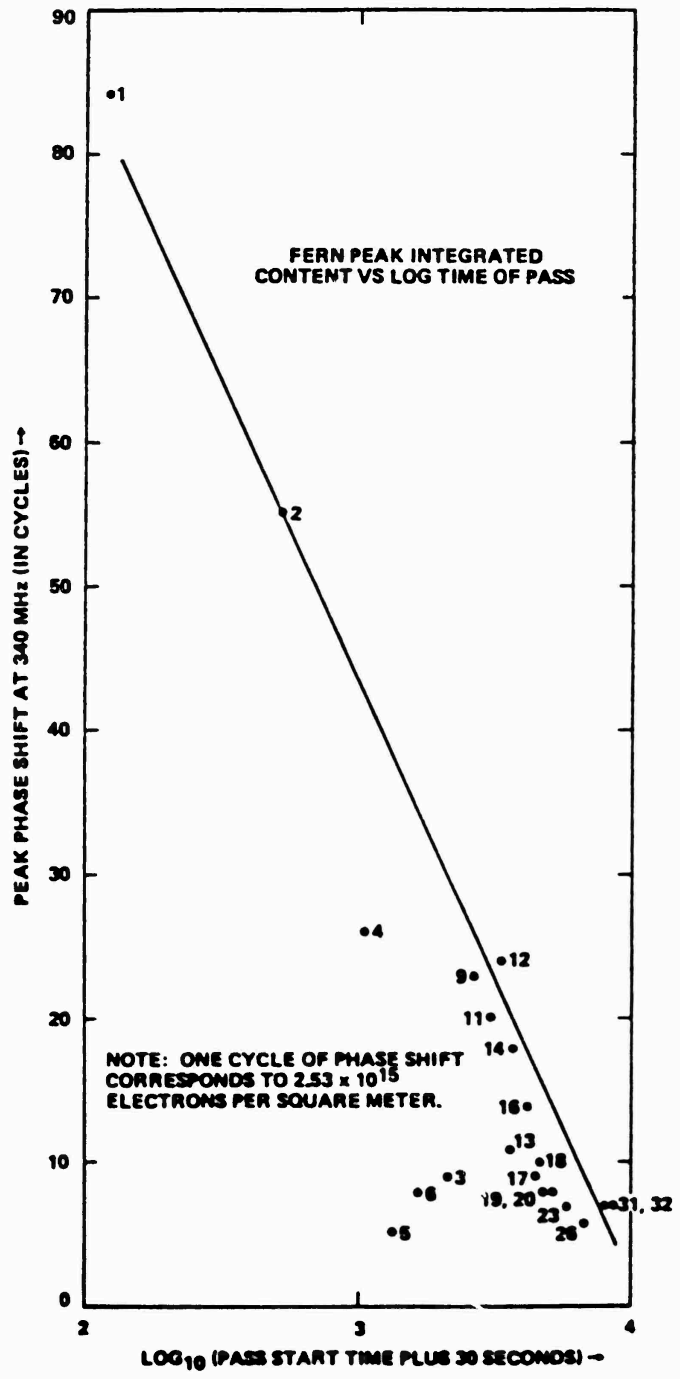

Figure 3-4. The decay of peak integrated electron content versus time after release observed in the FERN release of STRESS.

where J is the particle current density, μ is the ionic mobility in the surrounding air, B is the ambient magnetic field intensity of .4 gauss, N is the local ion density, and V_{slip} is the slip speed of this local density region with respect to the neutral cloud.

Because the current carriers are ions, currents into the barium cloud are carried by air ions and currents out of the ion cloud by barium ions. The barium ions associated with the plasma cloud are slowly replaced by air ions. Ion convection caused by currents is one basic feature of the proposed barium cloud decay mechanism. Note that if it were the only mechanism operative, that barium ion plasma clouds would gradually evolve into air ion plasma clouds. While the plasma RF effects would still be present they would not be associated with visible barium features. (This process was first noted by Linson in Kivel, Linson and Workman (1970).)

The second feature of the barium cloud decay mechanism is the chemical recombination of air ions. The mass spectrometer data from the AFGL probe payload flown during JAN (Narcisi, et al., 1981) shows that the molecular ion NO^+ is the predominant atmospheric ion below 190 km and thus at the barium cloud altitude. Because NO^+ has a very short lifetime in the elevated plasma cloud electron density, it recombines long before a significant air ion cloud is formed. The mass spectrometer data of AFGL reflects this fact showing virtually no NO^+ present in the ion cloud. Thus, the complete mechanism for ion cloud decay is that ions are convected out of the plasma cloud by plasma currents associated with the neutral wind and are replaced by molecular air ions which quickly recombine.

The decay time of an ion cloud can be approximated from the above current relation. The decay rate of a plasma column transverse to the field can be specified from the current in the column by

$$\frac{d\,N_T}{dt} = -|J| = -\frac{N_p}{\mu B}\,V_{slip}$$

where N_T is the columnar density, N_p is the peak density in the column and the remaining terms are as defined above. This relation predicts the observed dependence in the TEC decay seen in the PLACES and STRESS releases if N_p is proportional to $\frac{1}{t}$. Note that the predicted dependence of N_p from ambipolar diffusion (Linson, 1972) is $t^{-1/2}$ suggesting a close, but not exact, agreement. Thus at least qualitatively the decay of barium clouds can be explained by this mechanism.

A quantitative check of the mechanism reveals that it is very efficient. A column of constant density experiences ion removal at a rate equal to the slip speed divided by μB times the density. For typical parameters

$$\mu B = 10$$

$$V_{slip} = 20/ms$$

$$L = 6\ km$$

where L is the length of the column in the direction of the current, the cloud is completely depleted of barium in less than an hour! The mechanism is so efficient that the relevant question is no longer what makes barium clouds go away but rather what makes them last so long.

The proposed mechanism of decay not only explains the observed lifetime of barium, at least qualitatively, but it also explains an optical feature of the barium cloud observed in SECEDE II, STRESS and PLACES up the field views of ion clouds. In these views one side of the cloud typically has a very high contrast boundary that has been described as

"black aurora." The black aurora can be explained to be the side of the plasma cloud into which the plasma currents are convecting ambient air ions. On the other side of the cloud, currents are convecting barium ions out giving it a fuzzy optical appearance. The high contrast region, being more striking to the eye, is the feature which is singled out. This explanation gives good agreement with the observed slip directions and known geomagnetic field orientations.

3-3 BARIUM CLOUD SIMULATION

Numerical simulations of barium clouds can provide insight into cloud dynamics (Doles, et al., 1976, for example). A numerical simulation of the barium cloud has been performed to investigate the decay mechanisms presented in the previous section. This section discusses some of the results of this simulation.

The simulation models the barium cloud and the ionosphere with three constant altitude layers similar to Doles, et al. (1976). One layer corresponds to the E-layer, another layer corresponds to the barium cloud layer and the third layer corresponds to the F-layer. The initial densities on the E-layer and the F-layer are both assumed to be constant with values of 3×10^4 and 10^6 per cc respectively. The initial density of the barium cloud (Figure 3-5) is assumed to have a Gaussian spatial dependence with a 3×10^6 per cc peak density and a 3.9 kilometer e-folding radius. It is initially immersed in a constant background of NO^+ with density of 5×10^5 per cc.

A constant wind with a 50 meter per second velocity, directed horizontally and toward the right in Figure 3-5, is assumed to exist on all three layers. The equipotential

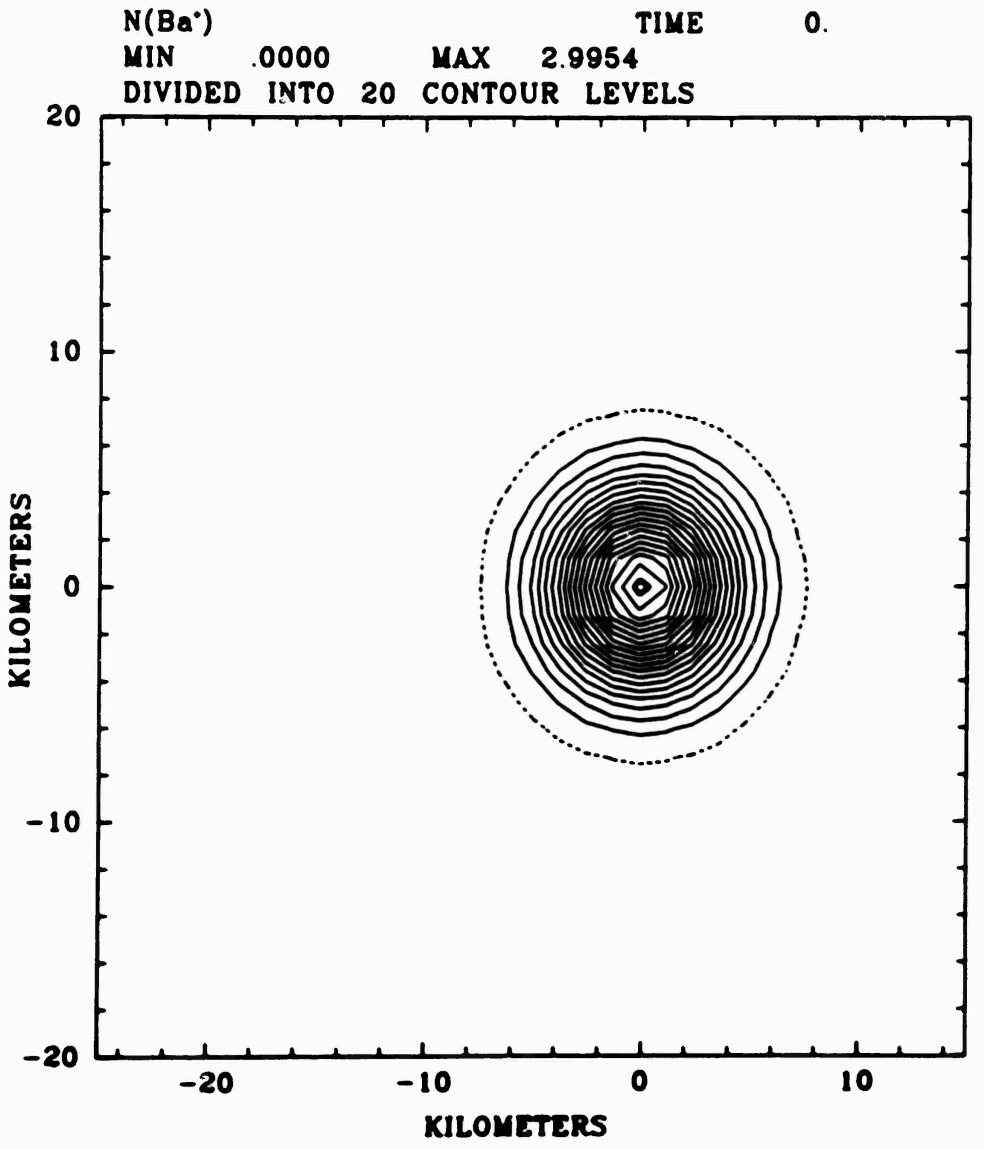

Figure 3-5. Initial barium density for numerical simulation.

approximation is used and the electric field on all three layers is assumed to have the same curl-free dependence. Both the Hall and Pedersen terms are included in expressions for the ion velocity and current. The expression for the current due to the ith species, J_i, is thus given by

$$\frac{J_i}{eN_i} = \frac{\mu B}{1 + (\mu B)^2}\left(\frac{E}{B} + V \times i_z\right) - \frac{1}{1 + (\mu B)^2}\left(\frac{E}{B} + V \times i_z\right)$$

where E is the electric field vector, V is the neutral wind velocity vector, i_z is the unit vector in the direction of the magnetic field, e is the electronic charge constant, N_i is the species density, B is the magnetic field intensity and μ is the ionic mobility in the background air. Note that μB is dimensionless and increases fairly rapidly with altitude because of the indirect proportionality between the mobility and the background neutral density. For the simulation the μB factor is assumed to be 1, 10, and 100 on the E-layer, barium layer, and F-layer, respectively. Note that the mobility of the barium and of the NO^+ on the same layer is assumed to be the same ignoring a factor of 2.5 which arises primarily because of the different ion masses.

A split-step approach is used in the simulation. The velocity field is determined from given density values by solving a potential equation for the electric field. The potential equation results from the specification that the divergence of the total current be zero in order to prevent charge accumulation. Given the velocity field, updated density values are then calculated from the continuity equation.

Figure 3-6 shows the electric field potential which has been calculated from the initial density profile. One feature of this plot is that the potential is not quite symmetric. The non-symmetry is the result of including Hall current terms in the total current expression. Another point to note is that free-space boundary conditions have been implemented in the potential solver. The solver assumes that there are no density gradients outside of the simulated region. The specification of artificial requirements for the potential values on the boundary has thus been avoided.

The effect of NO^+ recombination is modelled through the equation

$$\frac{d[NO^+]}{dt} = -.3\ [NO^+][Ba^+]$$

where the $[NO^+]$ and $[Ba^+]$ quantities are assumed to be in 10^6 per cc. The reaction reflects the recombination rates specified in the DNA Reaction Rate Handbook with the exception that the barium density has been used to approximate the electron density. This approximation is necessary to keep the background NO^+ from spontaneously decaying. The recombination step is applied after the convection step and just prior to the potential solving step. It has the effect of rapidly eliminating any NO^+ within the barium cloud.

The simulation scheme has been used to predict the densities on the various layers after hundreds of seconds of evolution using a 3 second time step. The predicted values at 300 seconds are shown in Figures 3-7 through 3-10.

Figures 3-7 and 3-8 show predicted values of the barium and NO^+ ions on the barium cloud layer. Note that the barium density has been distorted on the left hand side toward the bottom of the figure in the direction of the

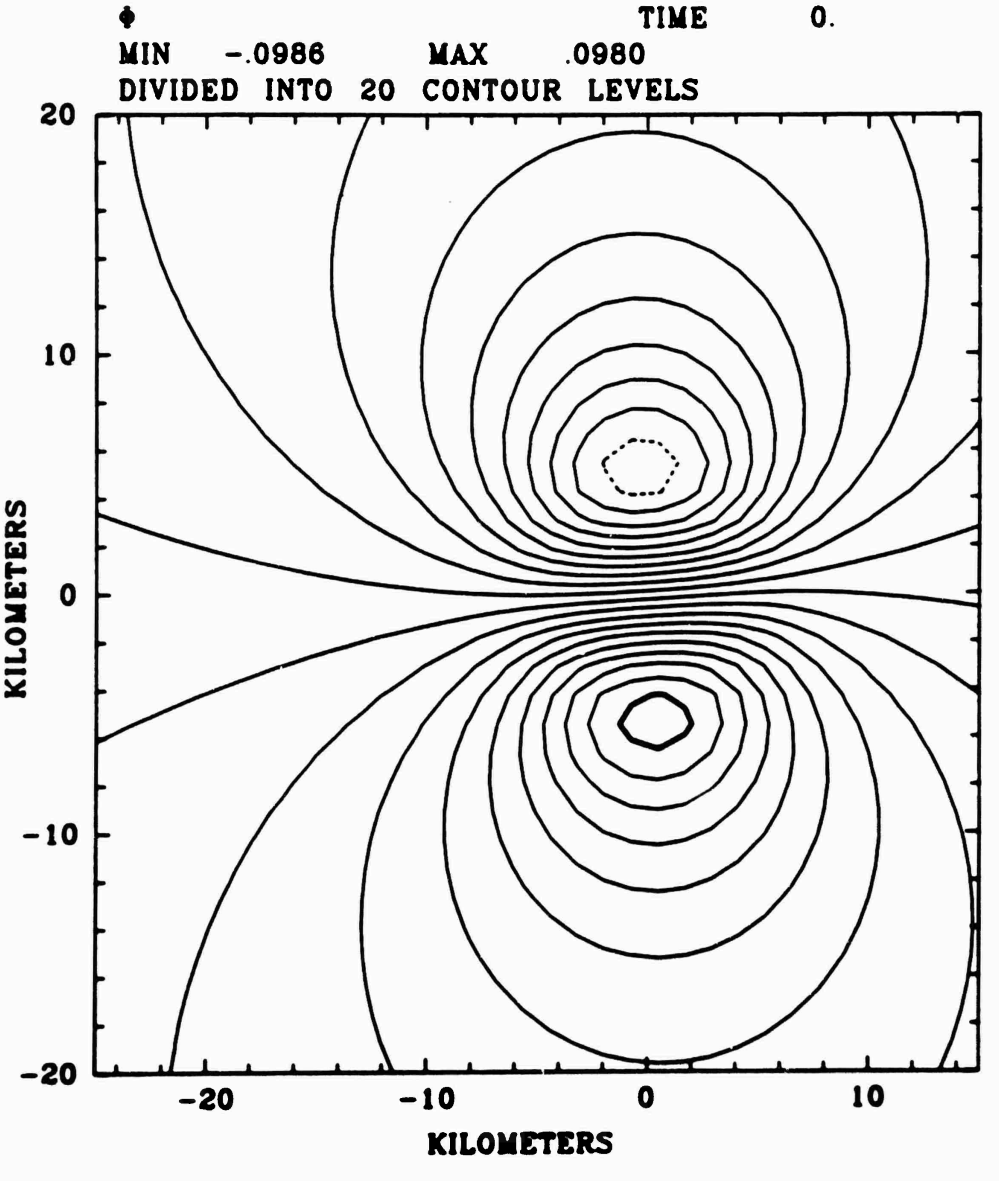

Figure 3-6. Electric field potential obtained from initial configuration. Free space boundary conditions are used. The assymmetry results from the inclusion of Hall current terms.

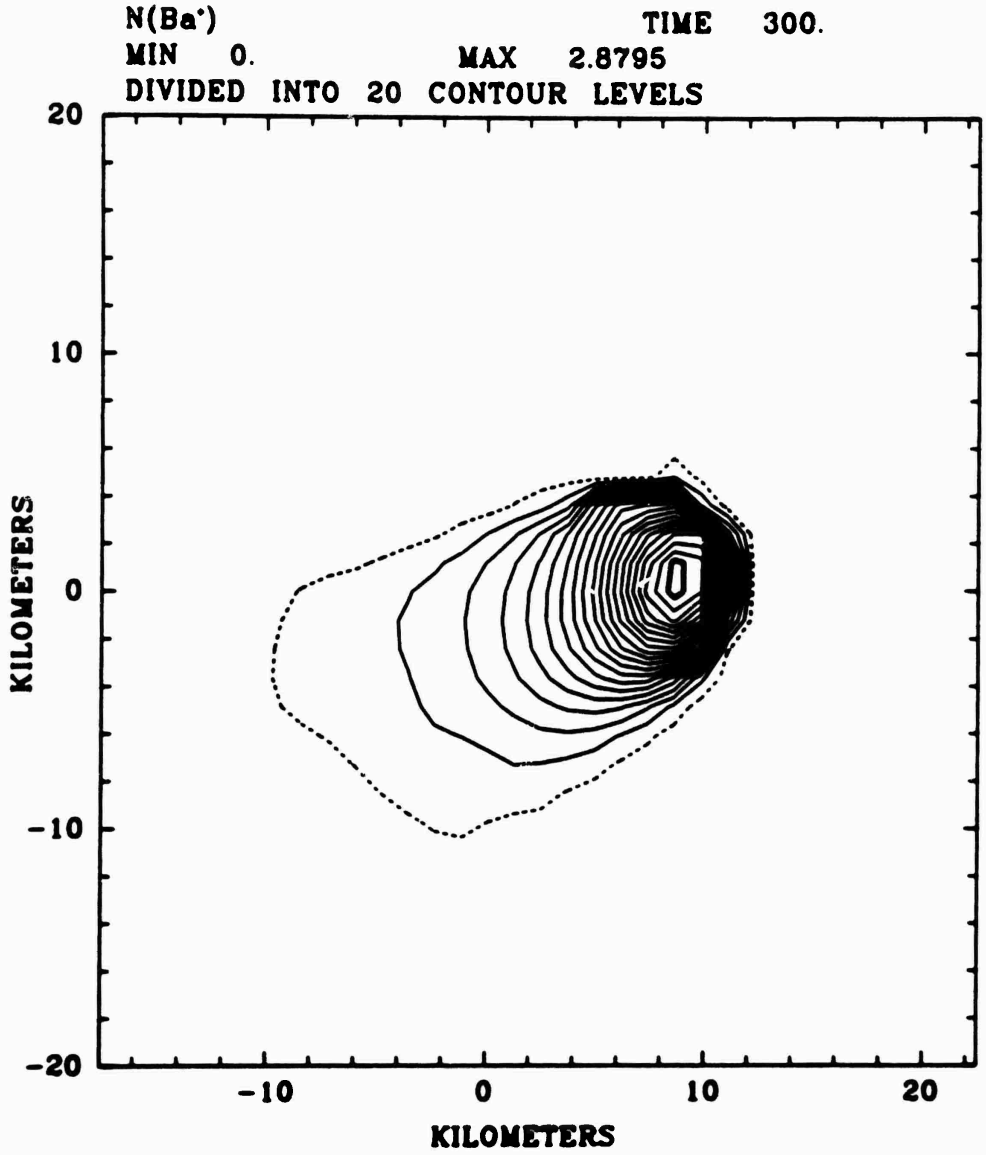

Figure 3-7. Barium ion density contours after 300 seconds of evolution. The downward motion is the result of Pedersen ion convection in the direction of the current.

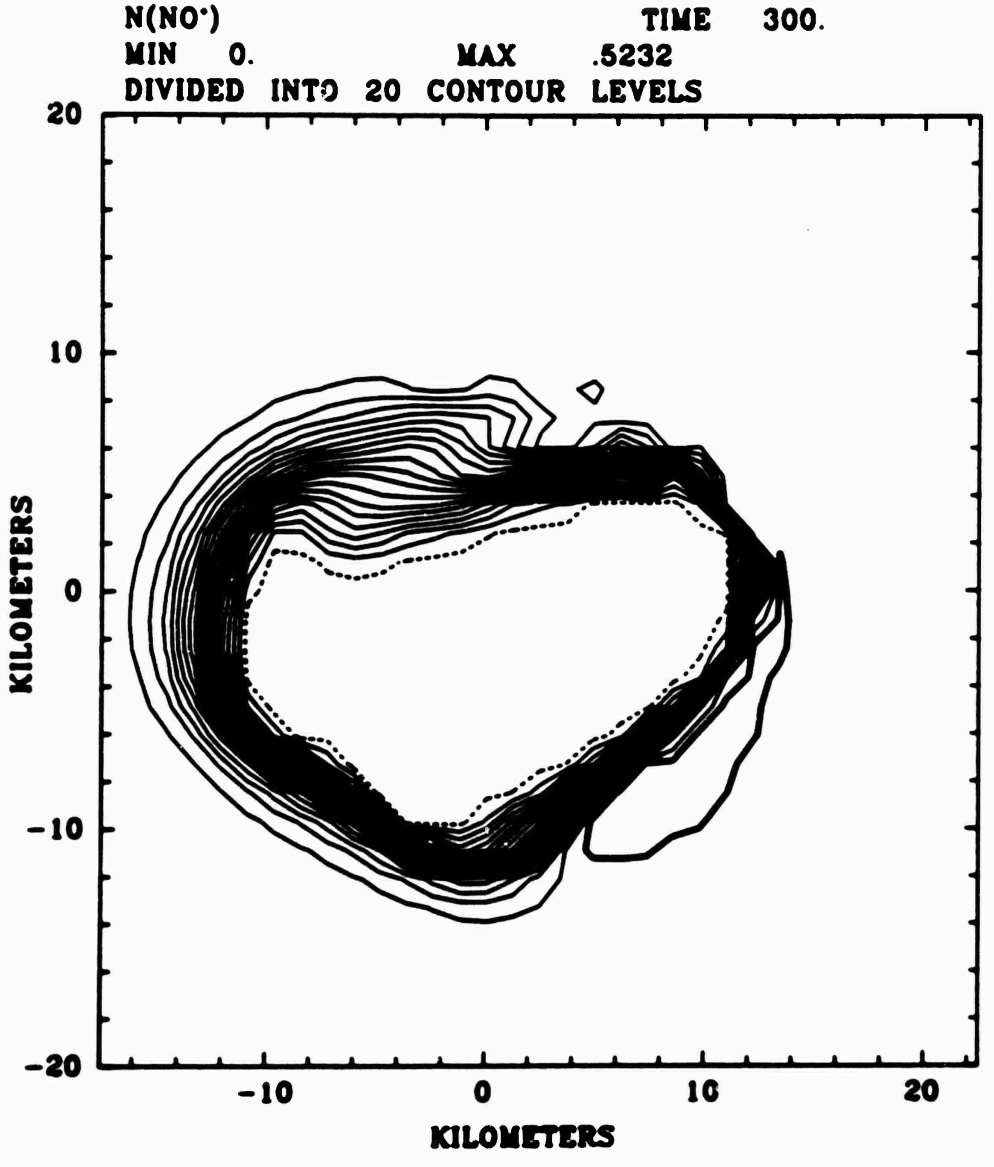

Figure 3-8. NO^+ ion density on barium layer after 300 seconds. Recombination has depleted a significant amount of NO^+ in central region.

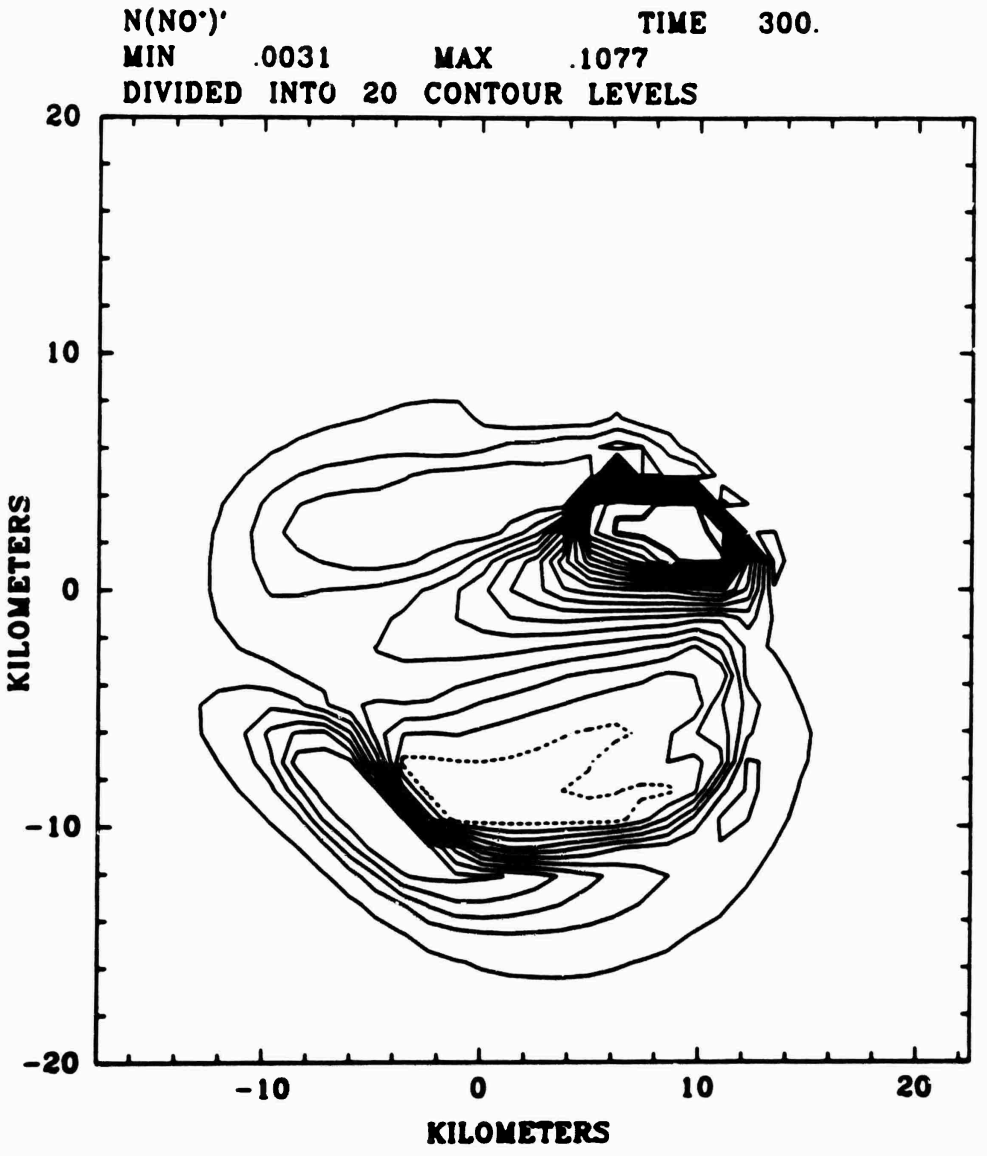

Figure 3-9. NO^+ ion density in E-layer demonstrating image enhancement and depletions. The density in the depletion is more than an order of magnitude less than its initial density.

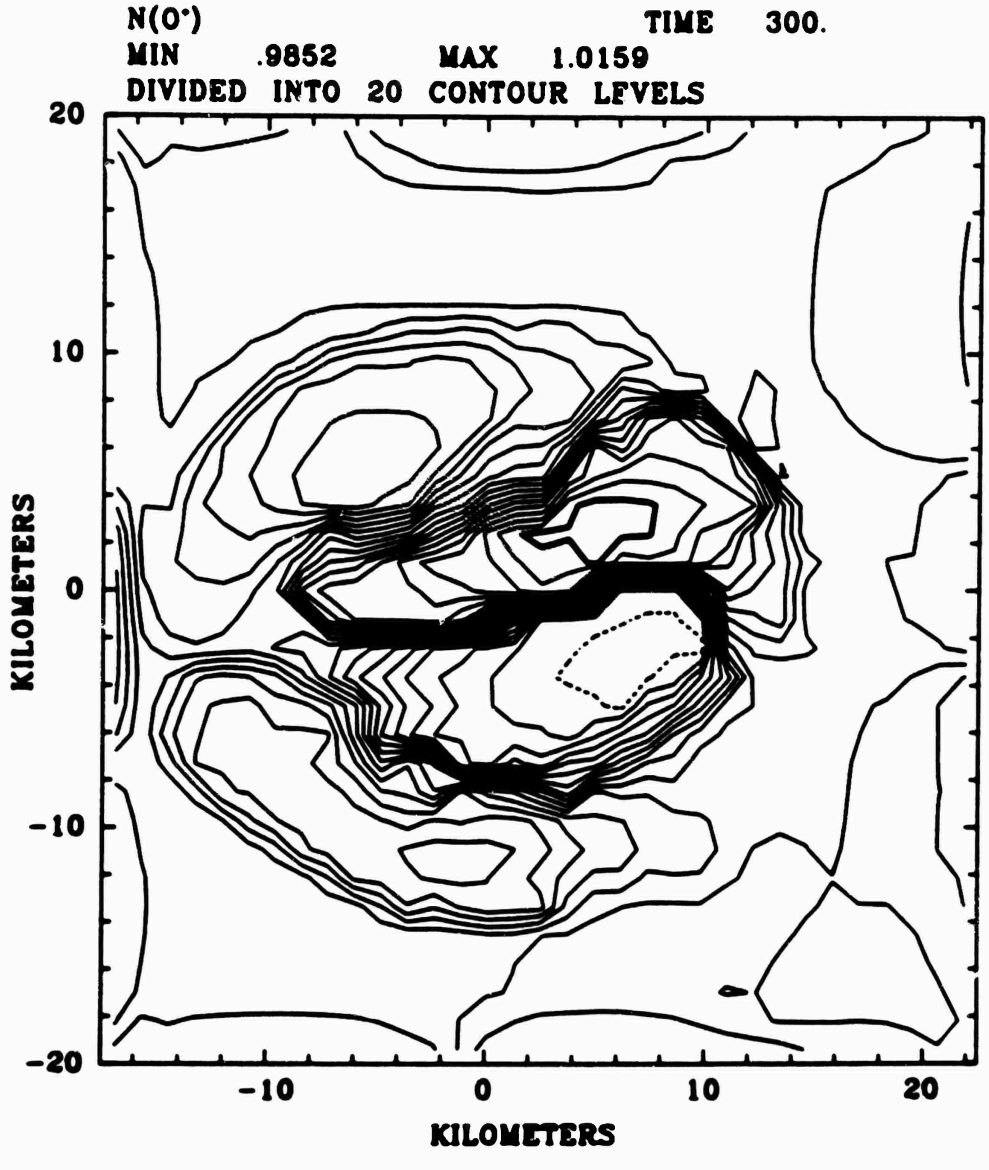

Figure 3-10. O^+ ion density in F-layer. The images in this region are much weaker on a percentage background basis than the E-layer images.

current. This distortion is a consequence of the ion convection performed by the current. The NO^+ density seen in Figure 3-8 shows that significant recombination has occurred. The interior density is nearly zero.

Figure 3-9 shows the density in the E-layer. The regions of significant enhancement and depletion of density are the image regions discussed in Doles, et al. (1976), Goldman, et al. (1974), and Scannapieco, et al. (1974). Because field aligned currents are carried by electrons and transverse currents are carried by ions three dimensional current flows can produce local regions of plasma enhancement and depletion. As illustrated in this figure these currents can even completely deplete the density from some regions.

Figure 3-10 shows the F-layer plasma density. Images are also evident in this region, however, their intensity relative to the assumed background O^+ density level is small. Image growth depends to a large extent upon the μB factor with large μB regions producing slower image growth. Recall that the μB factor is assumed to be 100 in this region in contrast to the factor of 1 assumed for the E-region. Because the density deflections produced are small, numerical noise is obvious near the boundary.

Figure 3-11 shows the field line integrated density. Because of the strong presence of the barium density the field line integrated Pedersen conductivity shown in Figure 3-12 is very similar. Note that the position of the peak field line integrated Pedersen conductivity is displaced somewhat in the vertical direction from that of the peak in the total field line integrated density, but the displacement is small. More striking is the difference between the total density and the field line integrated Hall conductivity seen in Figure 3-13. The Hall conductivity of the E-layer images

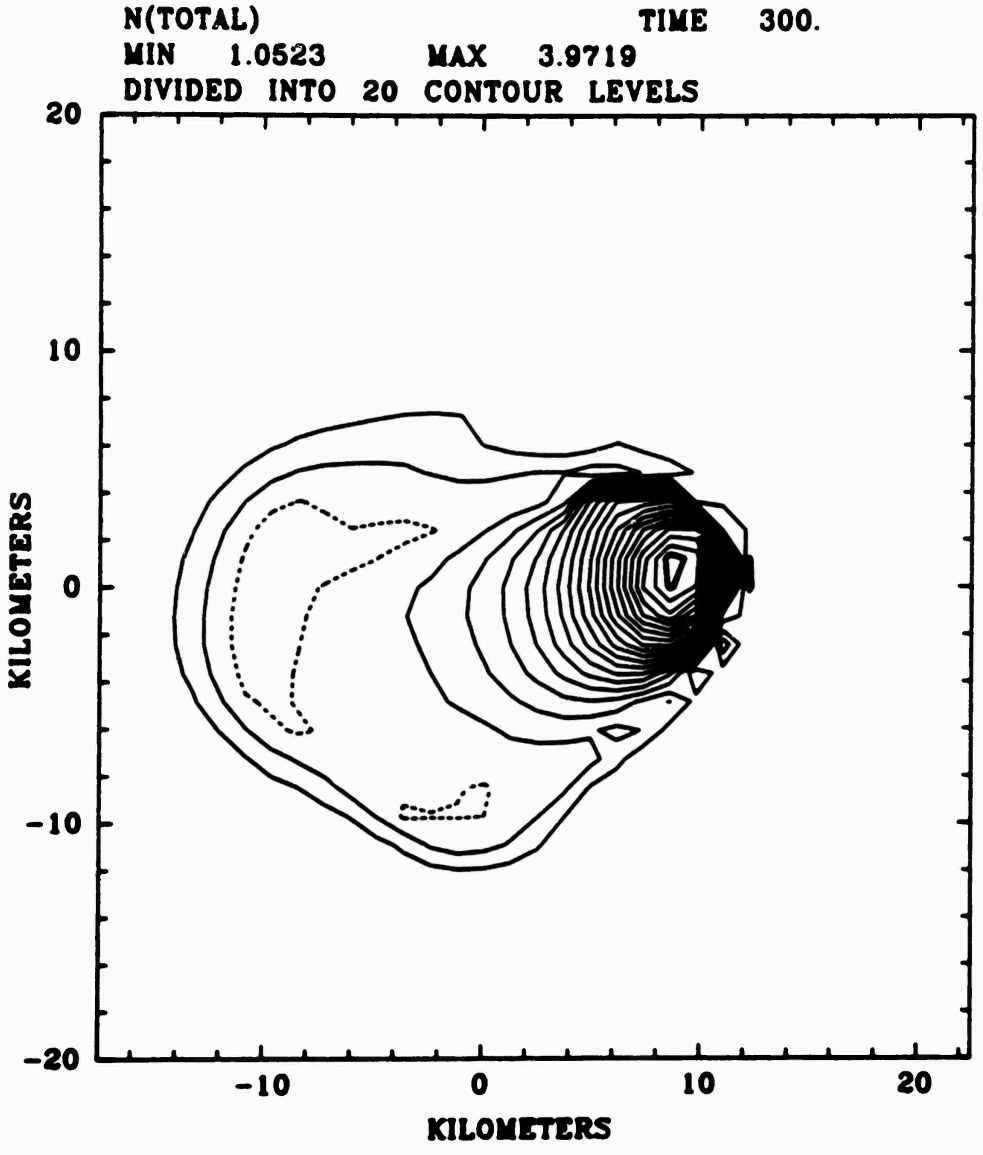

Figure 3-11. Field line integrated density at 300 seconds.

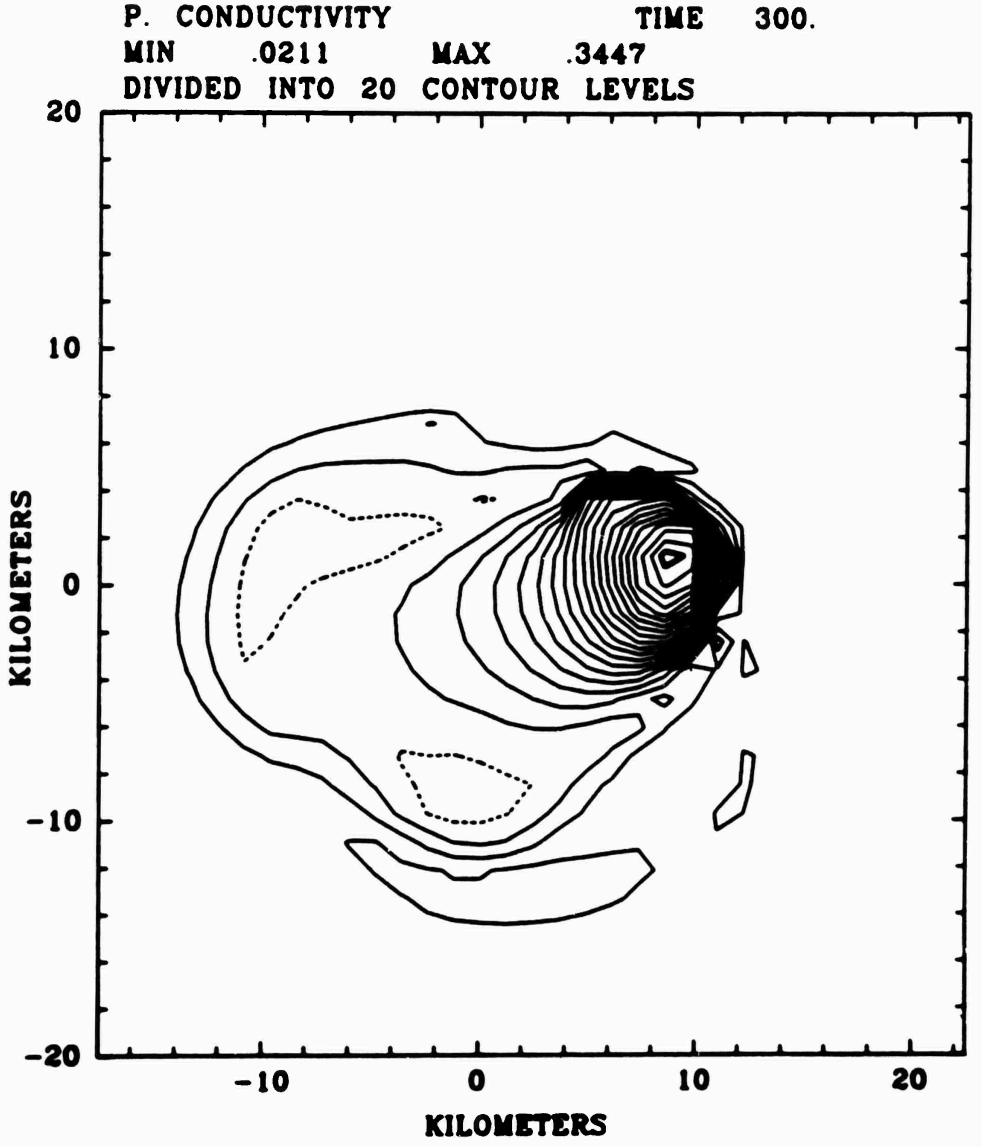

Figure 3-12. Field line integrated Pedersen conductivity at 300 seconds

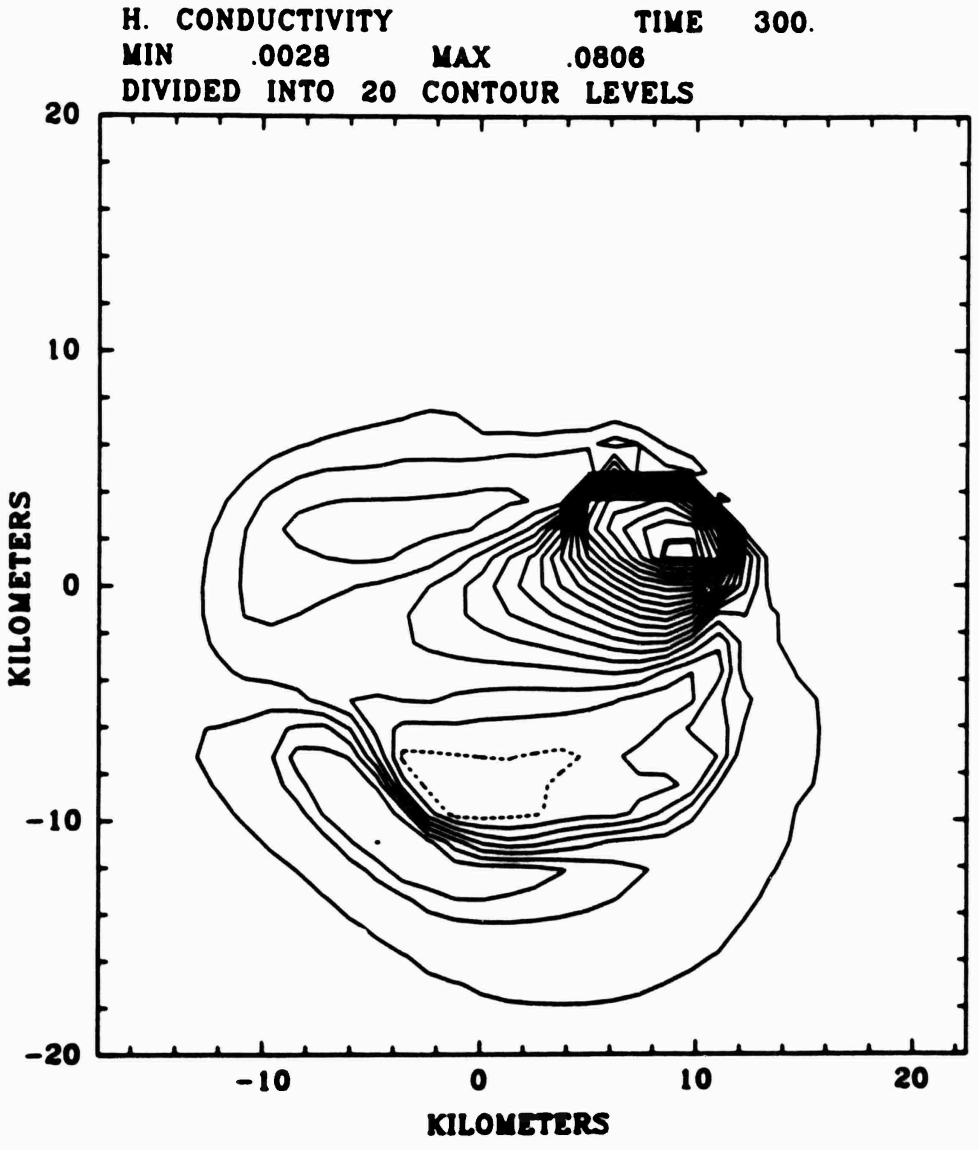

Figure 3-13. Field line integrated Hall conductivity after 300 seconds. The E-layer images are dominating the Hall conductivity.

is dominating the integrated Hall conductivity at this time. Figure 3-14 shows the electric field potential which results from these conductivities. It has evolved significantly from the original potential solution seen in Figure 3-6. The field has a distorted quadrupole nature at this time in place of its original dipole nature. The quadrupole nature of the potential field is indicative of the fact that contour stretching is occurring within the barium cloud. This stretching should (Linson 1981) eventually deform the leading edge of barium clouds into a long thin sheet thereby explaining the source of this type of feature which has been observed in the DIANNE density probe data from STRESS (Linson and Baxter, 1978).

The densities in each layer have been integrated in the two dimensions transverse to the field to display the TEC dependence expected in the backpropagated aircraft data. Figures 3-15 and 3-16 show the predicted integrated content of the barium layer including the background NO^+. The integration has been performed in the direction perpendicular to the wind in Figure 3-15 and in the direction parallel to the wind in Figure 3-16. Neither of the two plots seem to resemble backpropagated data because of the size of the TEC depletion regions. TEC depletion regions have not been observed in backpropagated data. This discrepancy may be due in part to the fact that depletions are traditionally considered erroneous artifact and the phase data has been framed to avoid such effects. An alternative cause for the discrepancy is that the barium ion density has been underestimated and the NO^+ ion density has been overestimated in the barium cloud layer region. Note that the depletion regions are associated with the NO^+ recombination processes and thus

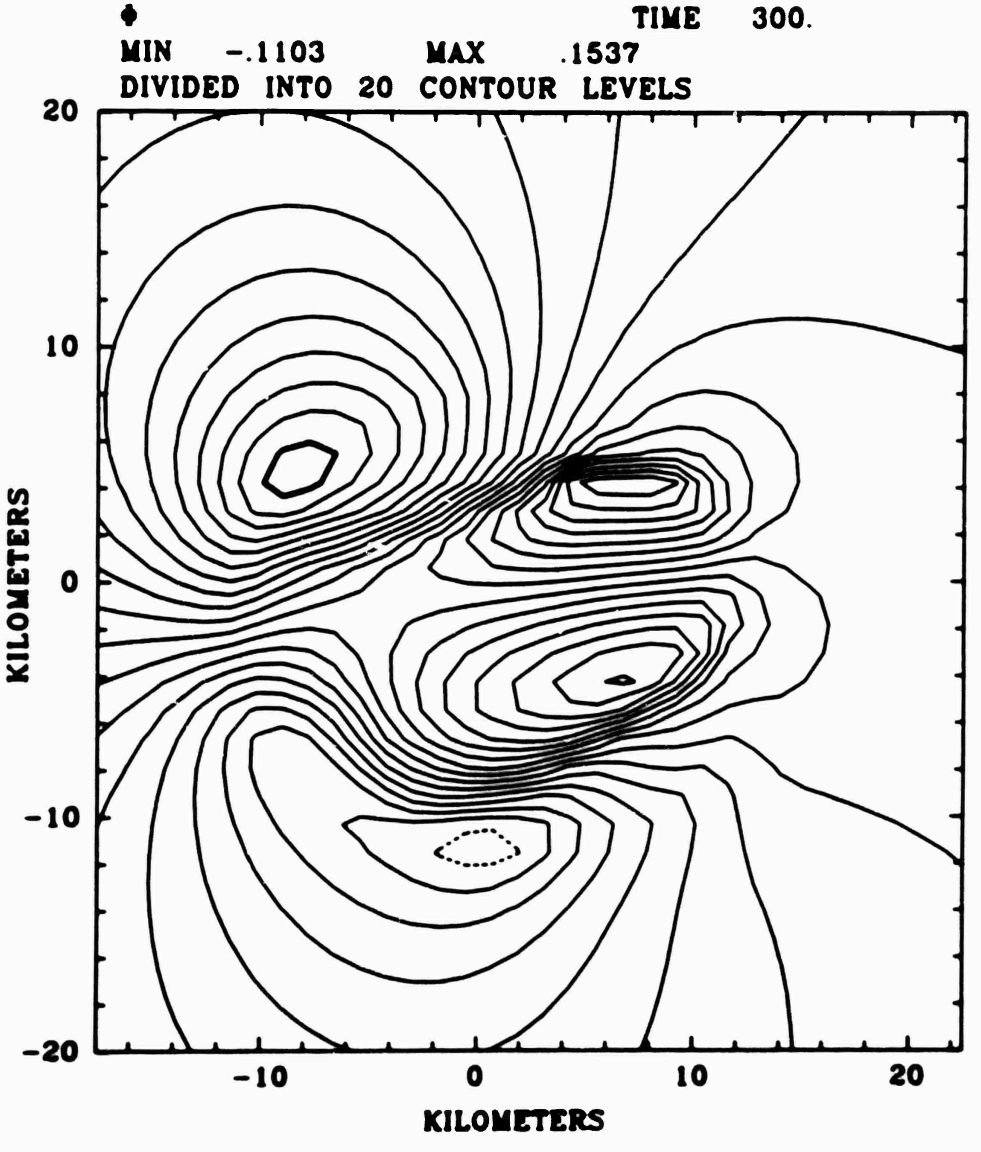

Figure 3-14. Potential solution at 300 seconds. A strong quadrupole like dependence is demonstrated.

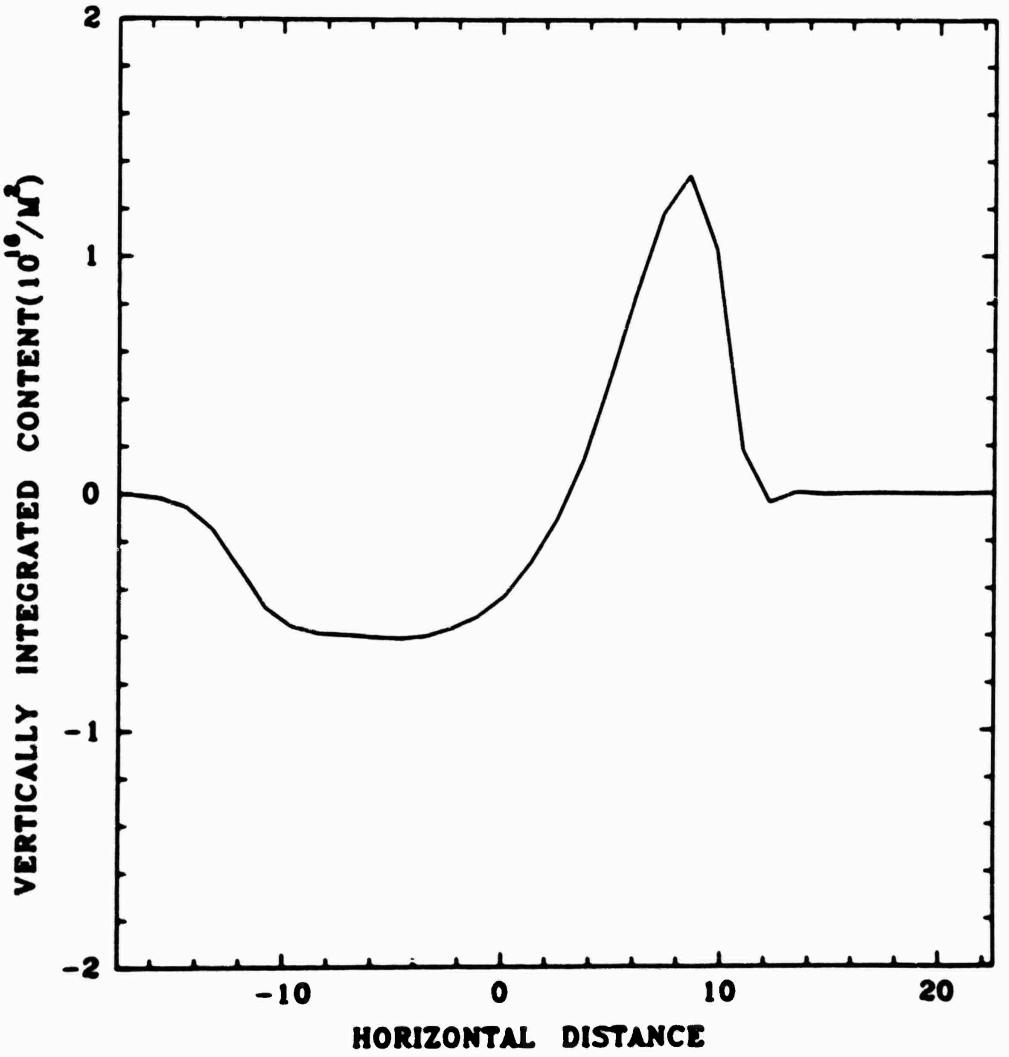

Figure 3-15. Total barium layer integrated content perpendicular to the wind.

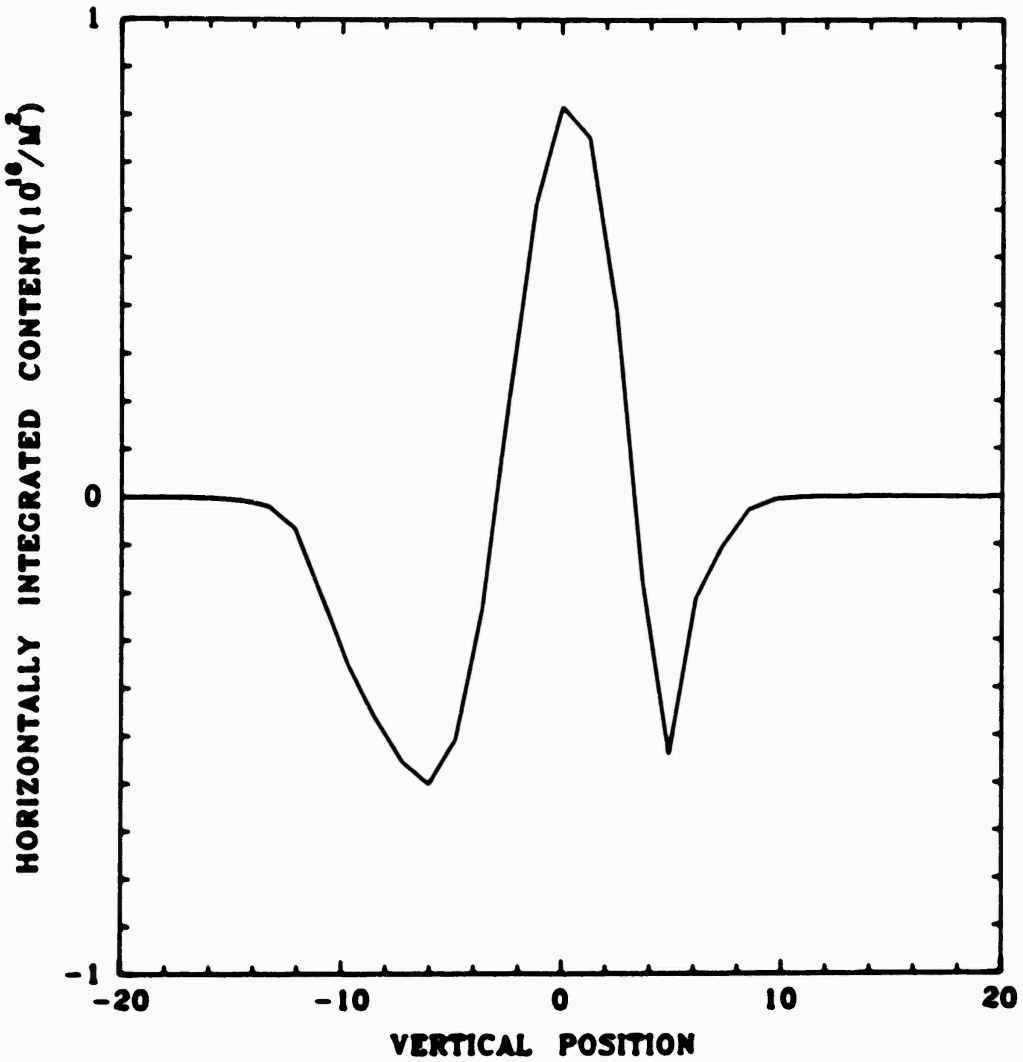

Figure 3-16. Total barium layer integrated content parallel to the wind.

errors in the local species densities or errors in the assumed chemistry process could produce the overexaggerated depletions in TEC.

Figures 3-17 through 3-20 show the predicted integrated content of the E-region and F-region for the two different integration directions. Note that the predicted intensities of these disturbances is very small. Each layer produces less than a cycle of UHF phase shift over kilometer distances. One distinctive feature of the predicted behavior which should be noted is the lazy 'S' like nature of the predicted curves. This feature should allow a distinction between barium cloud effects and the effects of cloud image regions.

The simulation was used to predict densities at times as late as 450 seconds. The results have been used to check the plasma decay rate. Figures 3-21 and 3-22 respectively show the decay of the peak TEC of the barium layer and the total loss of electrons from the plasma cloud. Once the NO^+ recombination associated with the initial barium plasma lay-down has subsided at roughly 40 seconds both quantities demonstrate a roughly linear loss rate. The decrease in TEC in the barium layer is roughly linear in spite of the fact that the barium cloud deformations associated with early time evolution are ongoing. Since the peak density of the barium is constant in the simulation, and not diffusing with a $t^{1/2}$ dependence as it would if ambipolar diffusion was included; the expected decay rate is constant. Thus these numerical results seem to be in good agreement with the decay rate relations set forth in the previous section.

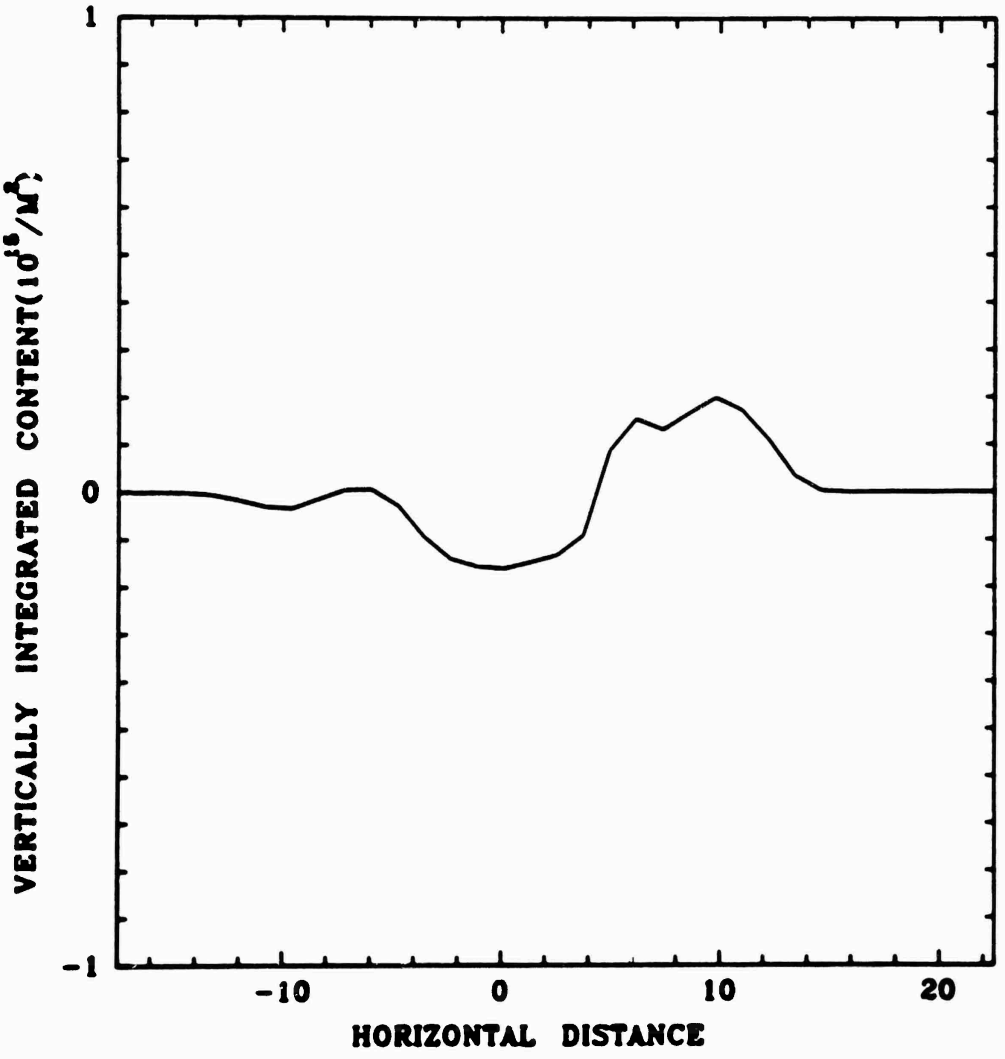

Figure 3-17. Column density of E-layer integrated in direction perpendicular to the wind.

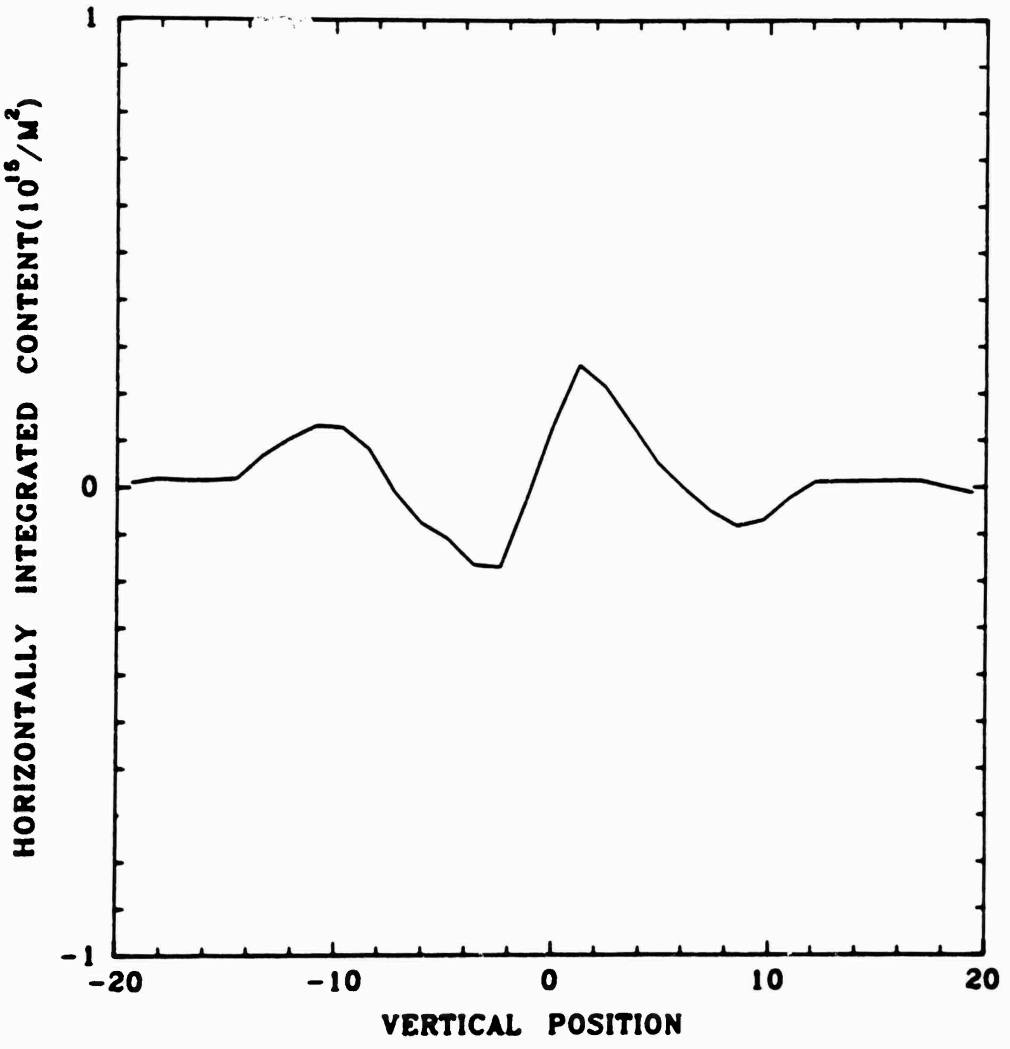

Figure 3-18. Column density of E-layer integrated in direction parallel to wind.

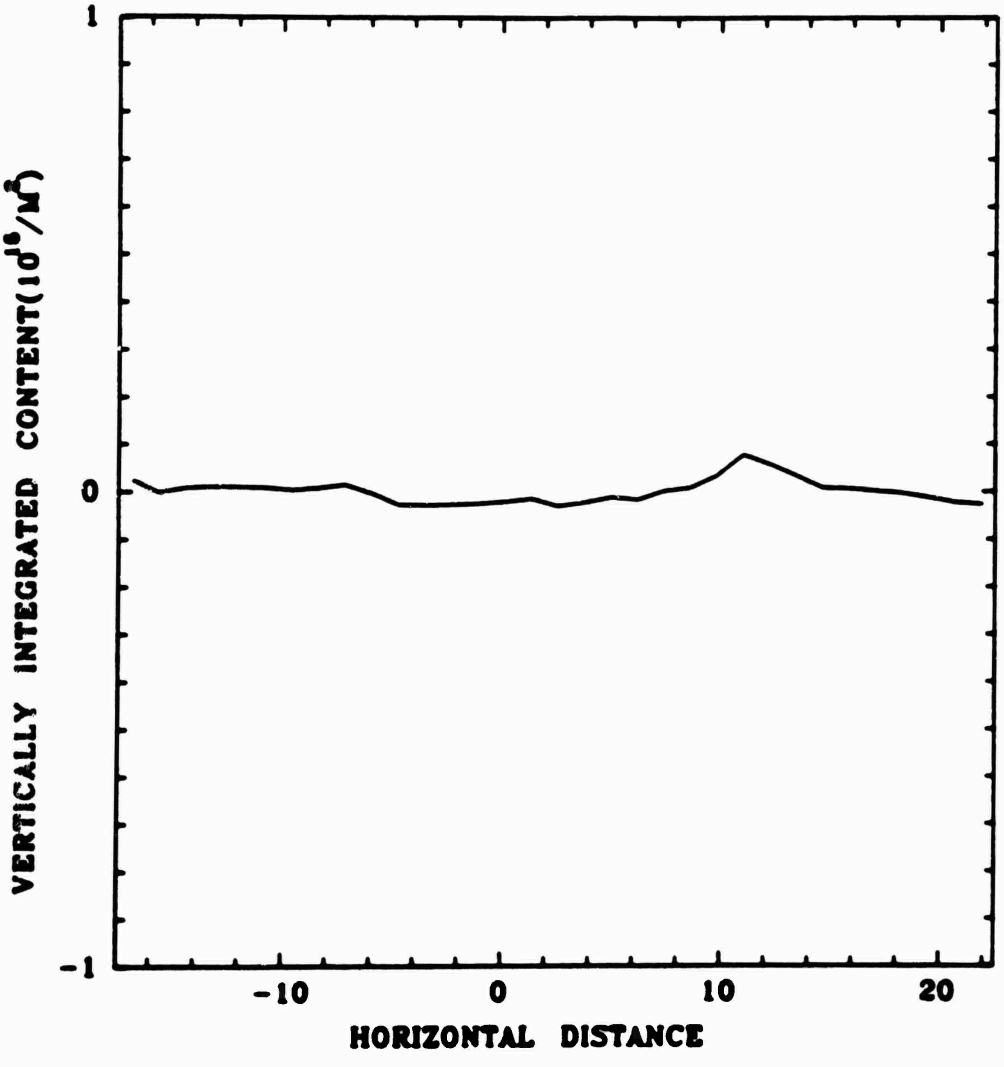

Figure 3-19. Column density of F-layer integrated in direction perpendicular to the wind.

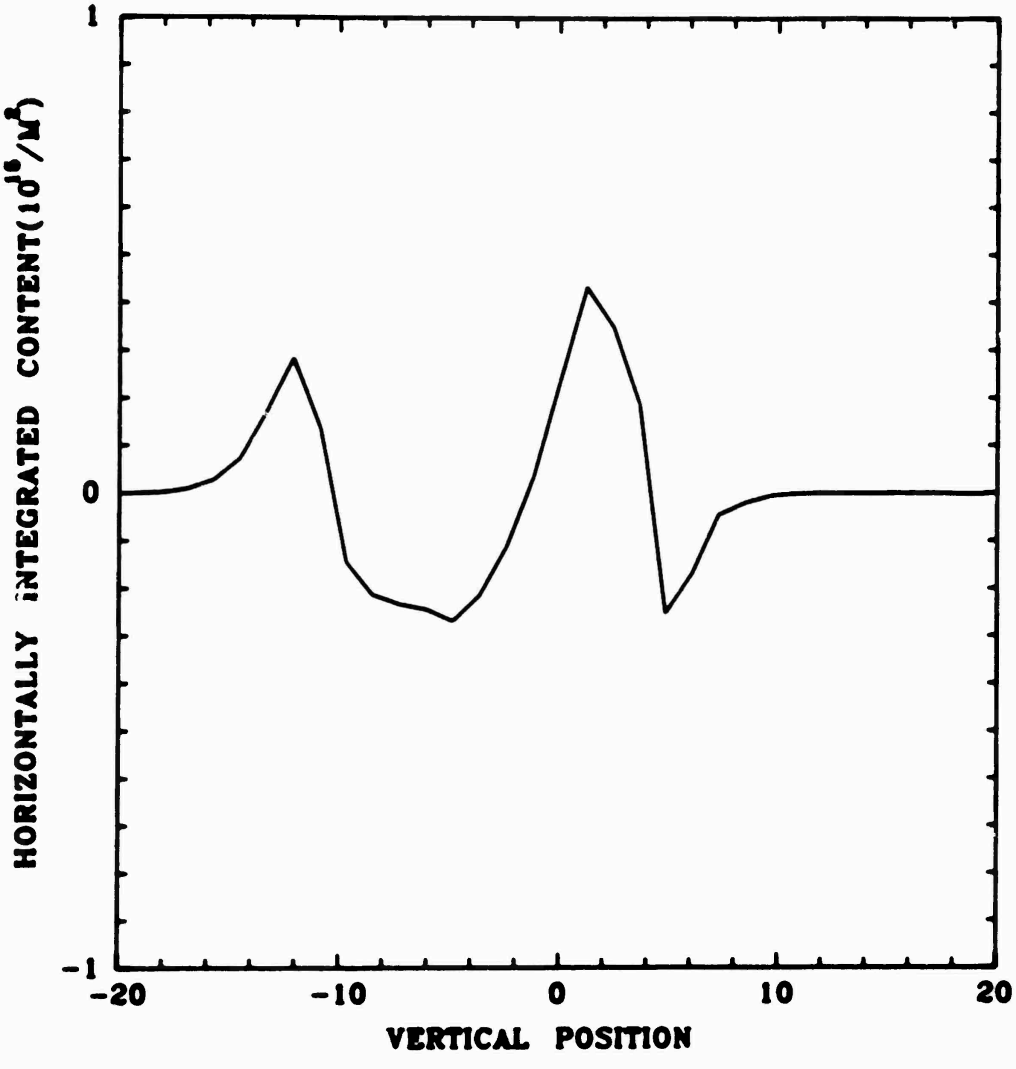

Figure 3-20. Column density of F-layer integrated in direction parallel to the wind.

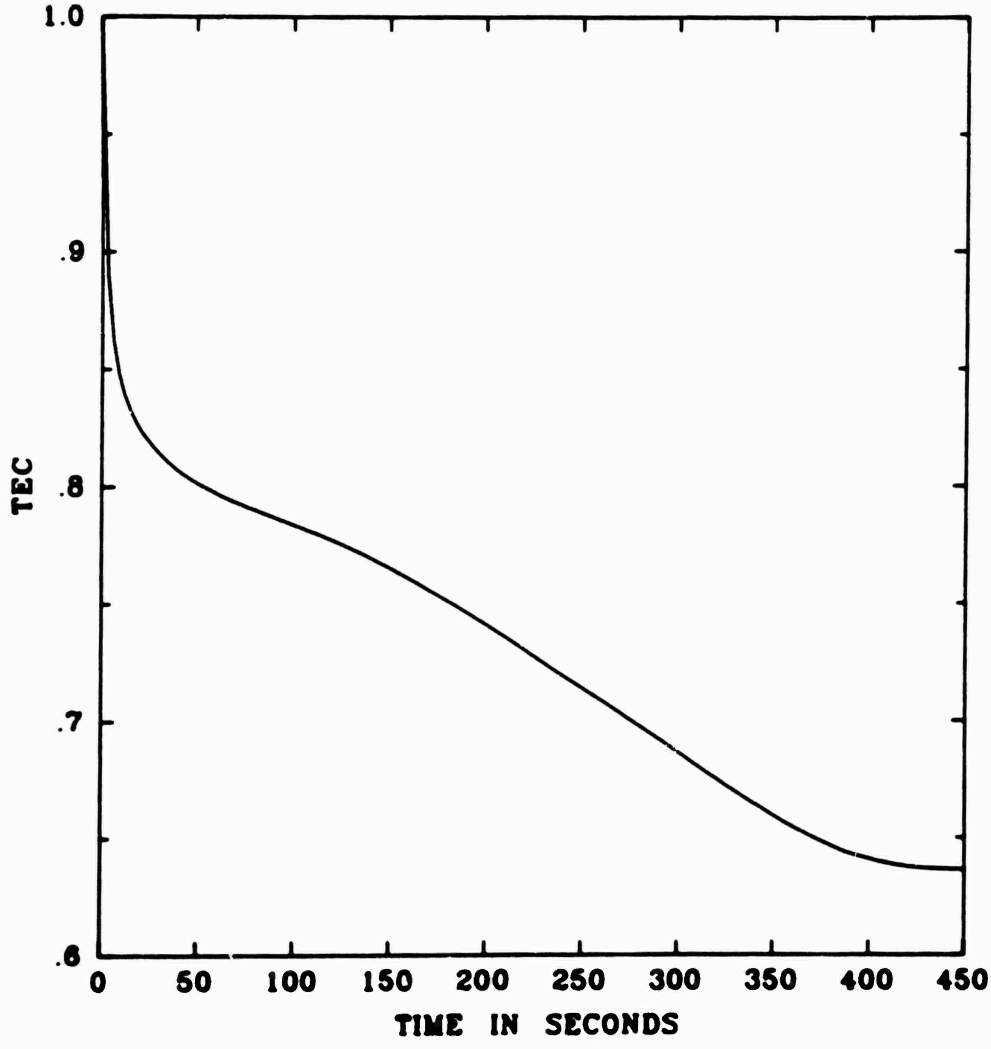

Figure 3-21. Peak value of total barium layer integrated content in the direction parallel to the wind vs time.

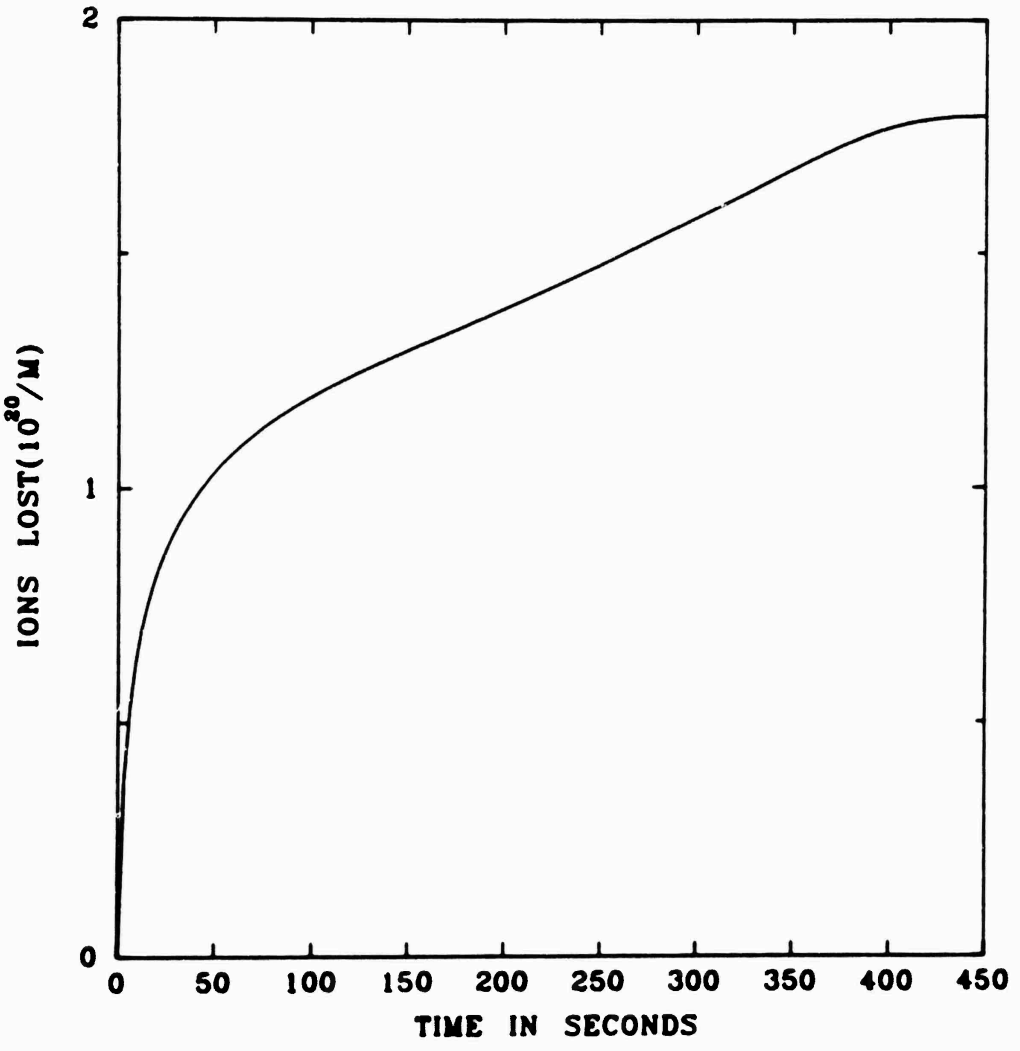

Figure 3-22. Loss of NO^+ versus time.

SECTION 4

NRL PROBE DATA ANALYSIS

During PLACES event JAN a payload which carried NRL plasma density measurement equipment was flown through the ion cloud. The plasma density was sampled at 4 kHz and the sample values were telemetered to a ground recording station. At the May 1981 PLACES data review meeting Szuszczewicz of NRL reported the results of the mean density measurements, which also appear in Szuszczewicz, et al. (1981), and the results of power spectral analysis. The power spectra of the density indicate the presence of a high frequency spur. This brief section describes the results of an attempt to track the frequency of this spur.

Data samples from the density probe were obtained from NRL with the goal of applying software frequency track techniques developed under a previous AFWAL effort (Prettie, 1981). The frequency track is of interest because its dependence can be used to identify the plasma wave which created the spur. For instance, a linear relation between the square of the wave frequency and the local density might suggest ion cyclotron waves as suggested by Szuszczewicz in his presentation.

No success was obtained in several attempts to lock the frequency tracking software onto the spur components in the density data. However, the raster scans which were generated in order to investigate the continuity and frequency dynamics of the spurs, produced useful results.

Figure 4-1 shows a raster scan plot generated from density data obtained while the probe was inside the barium cloud. Each horizontal trace is the amplitude in dB of a

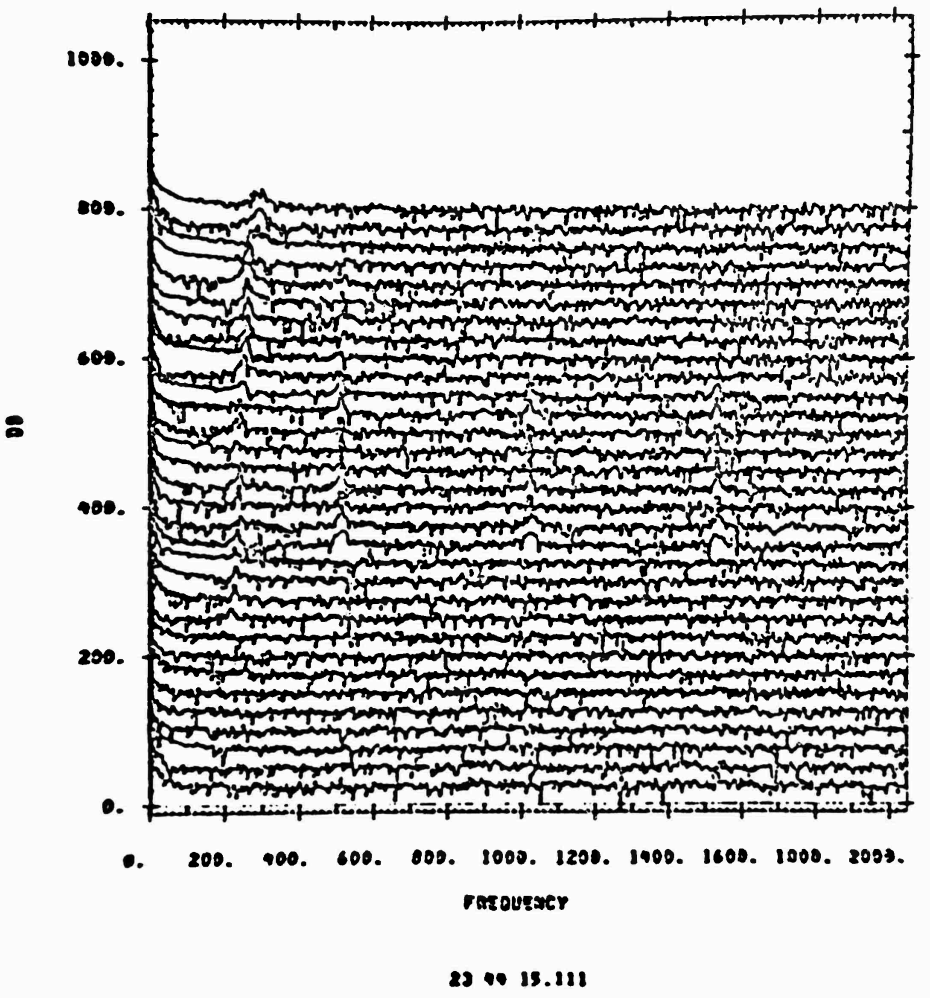

Figure 4-1. Raster scan plot showing presence of spectral spurs in barium density data. Each scan is FFT of 1/4 second of data. The plot covers 8 seconds total with time increasing vertically.

1024 point FFT of 1/4 second of data. Note that the dB scale of each trace is considerably compressed. The entire plot gives the traces of 32 contiguous records thereby covering 8 seconds in time or roughly 12 kilometers in distance. The start time for the first 1/4 second of data is 2344:15.1, its trace is at the bottom of the plot, and time progresses vertically. Evident in this plot are examples of spurs which can be seen near frequencies of 200 Hz. These spurs are persistent through roughly 6 seconds.

Plots similar to that seen in Figure 4-1 were generated for the entire set of data. Frequently no spurs were obvious in the results; however, when spurs were evident in the data, their frequency dependence with respect to the mean plasma density was characterized. The results of this exercise brought out the following important points:

1. Spectral spurs are evident when the payload is in the barium cloud.

2. Spectral spurs are also evident when the payload is 100 kilometers down-range from the barium cloud in the 200 kilometer altitude regime.

3. The frequency dependence of the waves show no clearcut dependence upon density. See Figures 4-2 and 4-3.

4. In one instance two spurs were observed to merge into one (Figure 4-4).

The above results are important for interpreting the spurs in terms of plasma waves. For example, these results indicate that the waves are not easily interpreted in terms of local ion plasma waves because their frequency dependence is not even monotonic with density and because it is difficult to explain the bimodal structure of the spectra

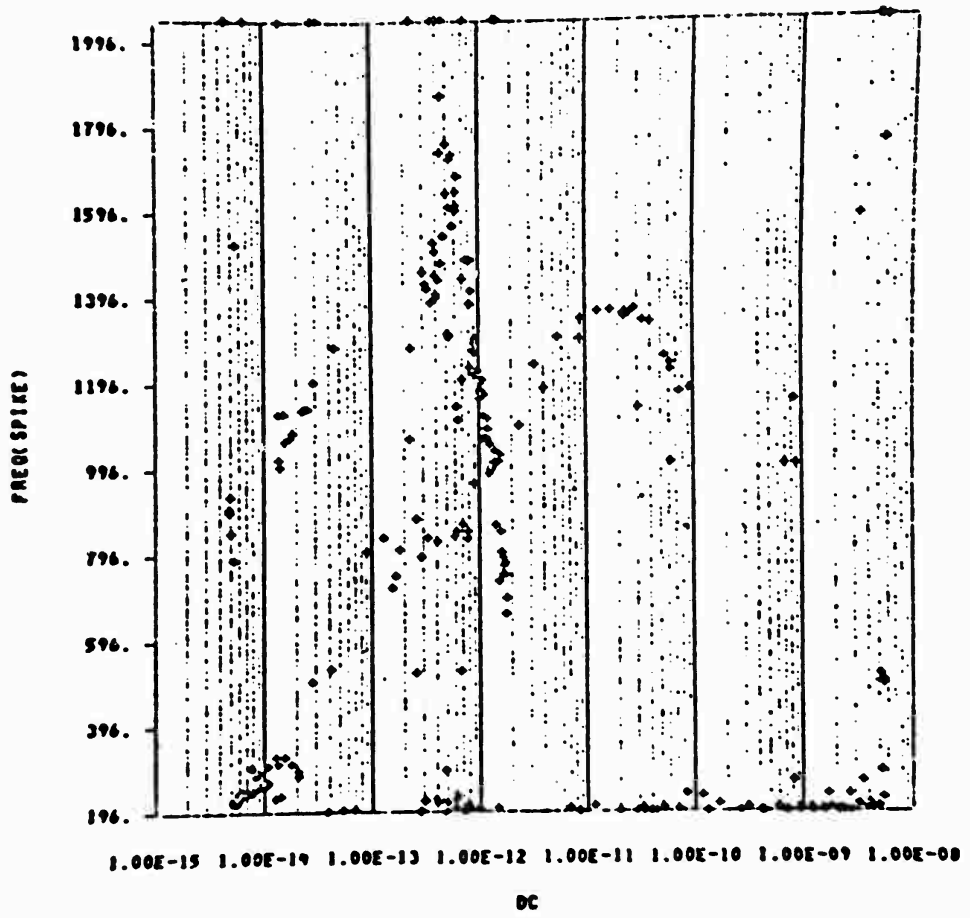

Figure 4-2. Frequency of spectral peak value versus DC from barium cloud region. The DC value is roughly proportional to local plasma density.

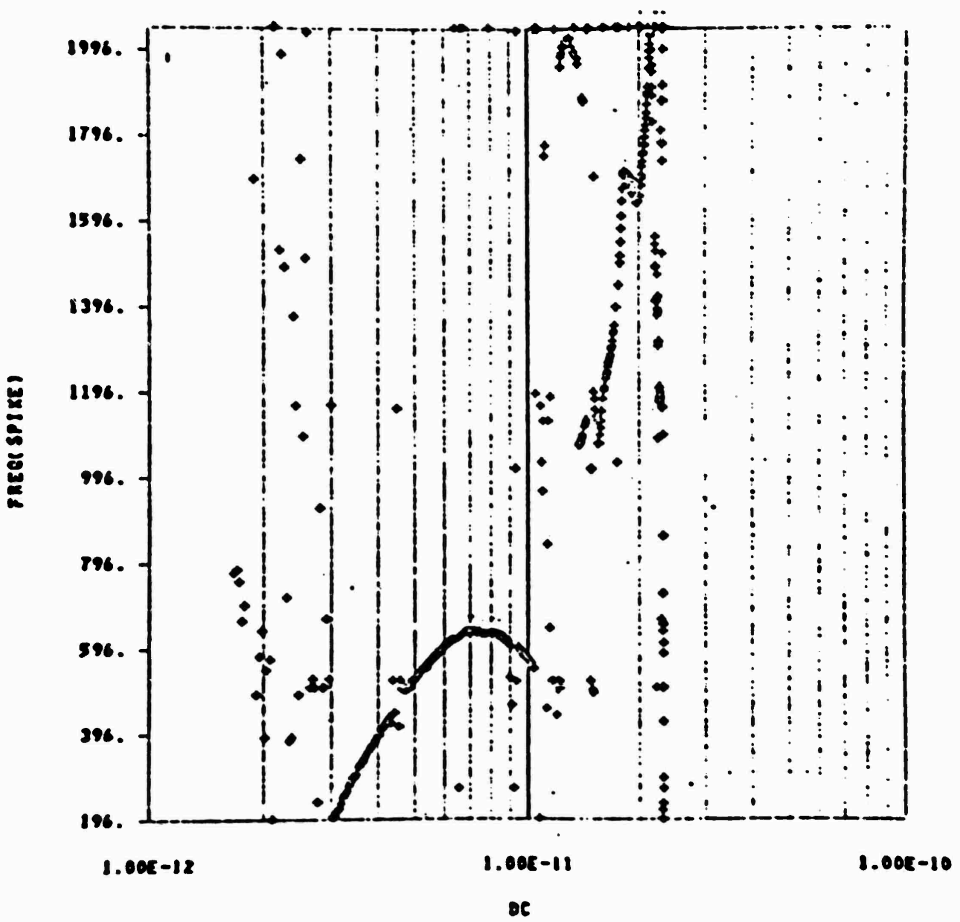

Figure 4-3. Frequency of spectral peak value versus DC value from F-layer. The DC value is roughly proportional to local plasma density.

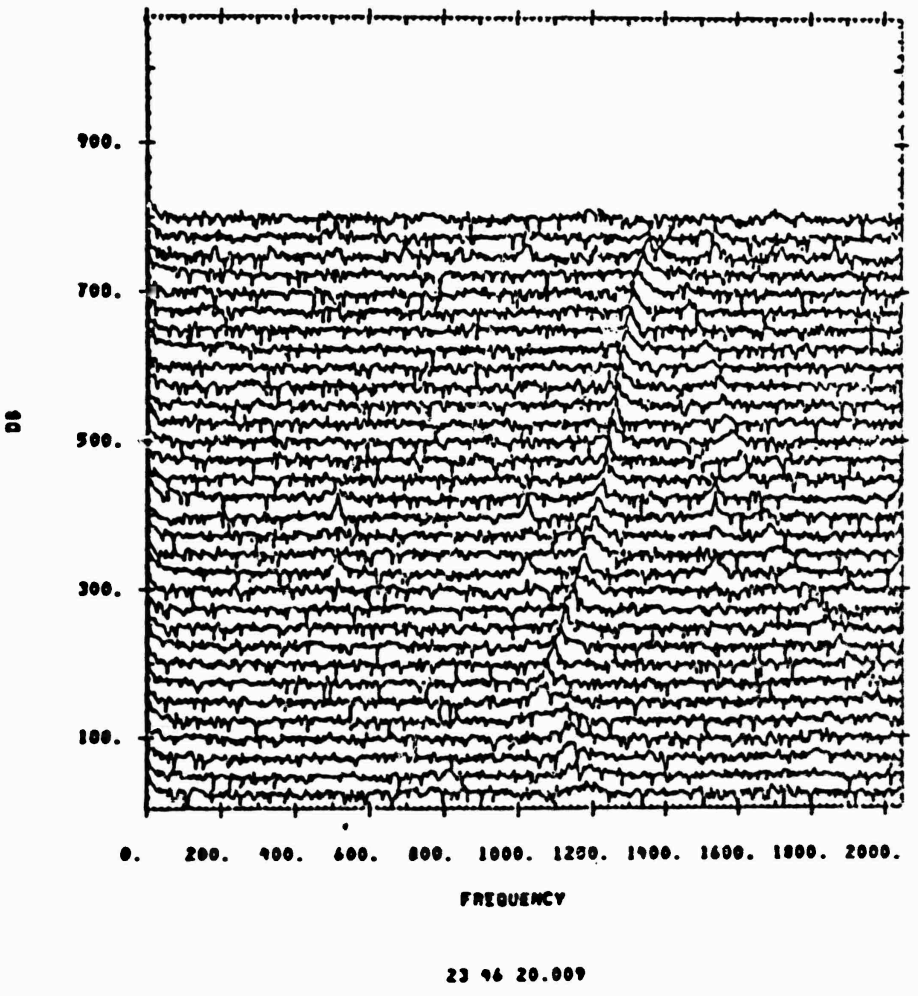

Figure 4-4. Raster scan plot showing the merging of two spectral spurs. The probe is well beyond the barium cloud at this time.

in terms of ion plasma waves. The phenomenological interpretation of the spurs is not known and beyond the scope of the effort; however, the above raster scan results should guide future plasma wave interpretations.

SECTION 5

CONCLUSIONS

The first goal of the PLACES experiment is the experimental verification of the propagation prediction techniques which determine HANE environment effects on pseudo-noise PSK systems. The second goal of the experiment is to develop further understanding of the phenomenology of the late-time evolution of structured ionospheric plasma. The results presented in this report demonstrate that these goals have been met.

Intense scattering of GHz pseudo-noise signals is expected from structured HANE environments. The scattering of the 100 MHz beacon payload signal measured from St. George Island is also intense and the effects observed have been used to rigorously test the theory in Section 2. The theory indicates that the scattering effects are closely described by geometry considerations. The theory predicts time-of-arrival delays and carrier phase sifts proportional to the dog-leg path increases in propagation distances. This feature of the theory has been tested by using the propagation results themselves , predict distances to the structure. Three different results have been used to obtain distance estimates, namely, 1) the wing-like behavior of the time-of-arrival of two isolated scattered signals versus time, 2) the doppler behavior of one isolated scattered signal versus time-of-arrival and 3) the doppler versus time-of-arrival dependence of the complete impulse response. The distance estimates obtained, namely, 28 and 32 km from 1), 30 km from 2), and 30 km from 3), are shown to be in excellent agreement with a geometric model of the structured ion cloud developed from

optical data. The geometric model indicates that structure should be between 10 and 42 kilometers from the beacon.

The development of the structure model from optical data is presented in Section 2. As part of the spin-off of this development other results of interest are available. The beacon occultation as viewed optically from St. George Island is shown and compared with the beacon data. Another result is that the wind shear rate vector is calculated. It is found to have a value of 1.5 meters per second per kilometer of altitude and a 351° azimuth.

Propagation data taken with instrumentation aboard the AFWAL 662 aircraft indicates a steady decay of TEC during PLACES event JAN. The decay took place through late time to 200 minutes after release. In Section 3 a two-step mechanism which explains this decay is presented. Barium is removed from the ion cloud by currents because in the ionosphere the carriers of currents transverse to the field are ions. The barium ions depleted from the ion cloud are replaced by ambient air ions which are predominantly NO^+ and which quickly recombine in the elevated plasma electron density because of their molecular nature. The net decay of the ion cloud is the end result. Quantitative predictions of cloud lifetimes indicate decay times of roughly 1 hour. To some extent the decay process might be impeded by image formation, however, this process is so efficient that it can easily explain the observed barium ion cloud decay behavior. Thus, an important understanding in the late-time phenomenology of ion clouds has been developed. A numerical simulation has been performed to incorporate the facets of this mechanism, and a gradual decay of the plasma cloud density has been demonstrated in the results, also presented in Section 3.

In Section 4 the results of a brief investigation of the NRL density probe data is presented. Szuszczewicz identified the presence of kHz spurs in the density power spectra as plasma waves existing within the barium cloud. The results shown in Section 4 indicate that the spurs occur on both the inside and outside of the ion cloud and do not have any apparent dependence on local density. At times the density power spectra are even bimodal.

Based on the results of this report the PLACES experiment can be viewed as a success. With experimental verification of the time-of-arrival effects associated with scattering, HANE propagation theory can be judged as well understood. New understanding of the late-time ion cloud phenomenology has also been obtained in investigations of experimental data. While phenomenological issues still remain and could be addressed by future ionospheric investigations, this should not detract from the significant milestones achieves by PLACES.

REFERENCES

_____, The American Ephemeris and Nautical Almanac; Washington, U.S. Government Printing Office, 1979, (Stock #008-054-00083-5).

J.H. Doles III, N.J. Zabusky, and F.W. Perkins, "Deformation and Striation of Plasma Clouds in the Ionosphere--3. Numerical Simulations of a Multilevel Model with Recombination Chemistry," Journal of Geophysical Research vol. 81, #34, December 1976, pp. 5987-6004.

S.R. Goldman, S.L. Ossakow and D.L. Book, "On the Nonlinear Motion of a Small Barium Cloud in the Ionosphere," Journal of Geophysical Research vol. 79, # 10, April 1974, pp. 1471-1477.

Dorrit Hoffleit with Carlos Jaschek, The Bright Star Catalogue, 4th revised edition, New Haven Connecticut, Yale University Observatory, 1982.

Kivel, Linson and Workman, Project SECEDE: Analysis of Barium Clouds in Chapter 2, "Nonlinear Barium Cloud Dynamics," RADC-TR-71-44, semiannual technical report, December 1970.

Lewis M. Linson, private communication, at Berkeley Research Associates, December 1981.

Lewis M. Linson, "Status of Theoretical Understanding of Barium-Ion-Cloud Phenomenology," AVCO Everett Research Laboratory in D.R. McDaniel, compiler, Proceedings of the SECEDE II Final Data Review Meeting, Vol. II, Stanford Research Institute, RADC TR-72-153, May 1972.

Lewis M. Linson and David C. Baxter, STRESS Ion Cloud Modelling, Science Applications, draft of Defense Nuclear Agency final report for contract DNA001-77-C-0047, August 1978.

James Marshall, Jeff Lehman, Gary Elston and Wayne Solbrig, PLACES Quick-Look Report for Beacon and Aircraft Experiments, ESL Inc., Defense Nuclear Agency Final Report, DNA 5737F, March 1981.

Dan R. McDaniel, compiler, Proceedings of the PLACES Preliminary Data Review Meeting, 20 and 21 May 1981, SRI International, Defense Nuclear Agency Proceedings, DNA 5848P, July 1981.

R. Narcisi, E. Trzcinski, G. Federico, L. Wlodyka and P. Bench, Composition and Structure Measurements in an Ionospheric Barium Cloud, Air Force Geophysical Laboratory, AFGL-TR-82-0003, December 1981.

Clifford W. Prettie, Phase Effects of Ionospheric Irregularities--Results of the Air Force Wright Aeronautical Data Processing Effort, Berkeley Research Associates, AFWAL technical report AFWAL-TR-81-1163, September 1981.

A.J. Scannapieco, S.L. Ossakow, D.L. Book, B.E. McDonald, and S.R. Goldman, "Conductivity Ratio Effects on the Drift and Deformation of F Region Barium Clouds Coupled to the E Region Ionosphere," Journal of Geophysical Research, vol. 79, #19, July 1974, pp. 2913-2916.

E.P. Szuszczewicz, J.C. Holmes, M. Swinney, and C.S. Lin, DNA/PLACES barium event JAN: Quick look field report on in-situ probe measurements, NRL Memorandum Report #4476, 1981.

B.T. Trombka and J.C. Cain, Computation of the IGRF--I. Spherical Expansions, Goddard Space Flight Center, NASA Report X-922-74-303, August 1974.

Harold B. Webb, Webb's Atlas of the Stars, 1940 (out of print).

Leon A. Wittwer, Radio Wave Propagation in Structured Ionization for Satellite Applications, Defense Nuclear Agency, in house report DNA 5304D, December 1979.

DISTRIBUTION LIST

DEPARTMENT OF DEFENSE

Defense Nuclear Agency
ATTN: STNA
ATTN: NAFD
ATTN: RAEE
ATTN: NATD
ATTN: RAAE, P. Lunn
3 cy ATTN: RAAE
4 cy ATTN: TITL

Defense Technical Information Ctr
12 cy ATTN: DD

Field Command Defense Nuclear Agency
Det 1
Lawrence Livermore Lab
ATTN: FC-1

Interservice Nuclear Wpns School
ATTN: TTV

DEPARTMENT OF THE ARMY

USA Nuclear & Chem Agcy
ATTN: Library

DEPARTMENT OF THE NAVY

Naval Research Lab
ATTN: Code 4720, J. Davis
ATTN: Code 4780
ATTN: Code 7500, B. Wald
ATTN: Code 4780, S. Ossakow
ATTN: Code 6700
ATTN: Code 7950, J. Goodman
ATTN: Code 4187
ATTN: Code 4700

DEPARTMENT OF THE AIR FORCE

Air Force Geophysics Lab
ATTN: OPR, H. Gardiner
ATTN: OPR-1
ATTN: LKB, K. Champion
ATTN: CA, A. Stair
ATTN: PHY, J. Buchau
ATTN: R. Babcock
ATTN: R. O'Neil

Air Force Technical Applications Ctr
ATTN: TN

Air Force Weapons Lab
ATTN: SUL
ATTN: NTYC
ATTN: NTN

Air Force Wright Aeronautical Lab
ATTN: A. Johnson
ATTN: W. Hunt

Air University Library
ATTN: AUL-LSE

DEPARTMENT OF ENERGY CONTRACTORS

Los Alamos National Lab
ATTN: MS 664, J. Zinn
ATTN: P. Keaton
ATTN: D. Simons
ATTN: MS 670, J. Hopkins
ATTN: T. Kunkle, ESS-5
ATTN: R. Jeffries
ATTN: J. Wolcott
ATTN: C. Westervelt

Sandia National Lab
ATTN: ORG 1250, W. Brown

DEPARTMENT OF DEFENSE CONTRACTORS

Aerospace Corp
ATTN: V. Josephson
ATTN: T. Salmi
ATTN: R. Slaughter
ATTN: I. Garfunkel
ATTN: J. Straus
ATTN: D. Olsen

Berkeley Research Associates, Inc
ATTN: J. Workman
ATTN: S. Brecht
4 cy ATTN: C. Prettie

Charles Stark Draper Lab, Inc
ATTN: A. Tetewski
ATTN: J. Gilmore
ATTN: D. Cox

ESL, Inc
ATTN: R. Ibaraki
ATTN: R. Heckman
ATTN: J. Lehman
ATTN: E. Tsui
ATTN: J. Marshall

General Research Corp
ATTN: B. Bennett

Geo-Centers, Inc
ATTN: E. Marram

JAYCOR
ATTN: J. Sperling

Kaman Tempo
ATTN: B. Gambill
ATTN: DASIAC
ATTN: J. Devore
ATTN: W. Knapp
ATTN: K. Schwartz
ATTN: W. McNamara

MIT Lincoln Lab
ATTN: D. Towle

Pacific-Sierra Research Corp
ATTN: H. Brode, Chairman SAGE

DEPARTMENT OF DEFENSE CONTRACTORS (Continued)

MA/COM Linkabit, Inc
ATTN: H. Van Trees
ATTN: A. Viterbi
ATTN: I. Jacobs

Mission Research Corp
ATTN: R. Hendrick
ATTN: C. Lauer
ATTN: R. Kilb
ATTN: F. Fajen
ATTN: R. Bigoni
ATTN: G. McCartor
ATTN: F. Guigliano
ATTN: Tech Library
ATTN: S. Gutsche
ATTN: R. Bogusch

Physical Dynamics, Inc
ATTN: E. Fremouw

Physical Research, Inc
ATTN: R. Deliberis

R&D Associates
ATTN: R. Lelevier
ATTN: C. Greifinger
ATTN: R. Turco
ATTN: H. Ory
ATTN: W. Wright
ATTN: M. Gantsweg
ATTN: W. Karzas
ATTN: F. Gilmore

R&D Associates
ATTN: B. Yoon

DEPARTMENT OF DEFENSE CONTRACTORS (Continued)

Rand Corp
ATTN: E. Bedrozian
ATTN: C. Crain

Science Applications, Inc
ATTN: L. Linson
ATTN: C. Smith
ATTN: E. Straker
ATTN: D. Hamlin

SRI International
ATTN: G. Price
ATTN: R. Tsunoda
ATTN: J. Vickrey
ATTN: W. Chesnut
ATTN: R. Livingston
ATTN: D. Neilson
ATTN: J. Petrickes
ATTN: D. McDaniels
ATTN: R. Leadabrand
ATTN: M. Baron
ATTN: A. Burns
ATTN: C. Rino
ATTN: G. Smith
ATTN: V. Gonzales
ATTN: W. Jaye

Sylvania Systems Gp
ATTN: J. Concordia
ATTN: I. Kohlberg

Visidyne, Inc
ATTN: C. Humphrey
ATTN: O. Shepard
ATTN: W. Reidy
ATTN: J. Carpenter